学 位 論 文

ファンデルワールス界面の作成・構造・物性
に 関 す る 研 究

平成 5 年 11月 博士（理学）申請

東京大学大学院理学系研究科
化 学 専 攻

島 田 敏 宏

# Contents

# PREFACE

Today we experience the historical moment when the size of the objects in electronics processing and in solid state chemistry coincides at the nanometer scale. One of the active fields in nano-science / technology is microfabrication applying controlled surface crystal growth. It utilizes surface science and ultrahigh vacuum technologies which have been developed in the last three decades. Molecular beam epitaxy (MBE) is one of these technologies, by which it is possible to fabricate single crystalline films controlled in each atomic layer.

MBE has been a great success in both of practical application and pure science. New electronic devices, including the high electron mobility transistor, are already utilized commercially for ultra high frequency applications. Novel phenomena arising from hetero-interfaces such as quantum hall effect have improved the accuracy of fundamental constants in physics. Atomically abrupt and single crystalline interfaces were essential in these applications of MBE. These interfaces are only obtained from a few number of materials among compound semiconductors of III-V groups. Covalent chemical bonds which exist at the interfaces limit the combination of materials.

MBE of layered materials has been introduced to the science community by Prof. Koma as van der Waals epitaxy (VDWE) to circumvent that limitation. Since surfaces of layered materials have no dangling bonds, it is expected that the interfaces fabricated by VDWE are combined by van der Waals forces without covalent chemical bonds. In other words, this material system has the nature of molecular crystals in one of the dimension perpendicular to the layers. Due to the wide selection of the electronic and optical properties in layered materials, VDWE provides an opportunity for the study of the novel interfaces consisting of materials with quite different properties.

In the present study, two fundamental problems in solid state physics and chemistry of layered materials have been investigated by applying VDWE and surface science techniques. One is charge density waves (CDWs) in metallic layered materials and the other is structural polytypes. Novel results have been obtained for both of these issues.

wishes to express his thanks to the members of Prof. Koma's group for useful discussions on various fields of science.

# Chapter 1. Introduction

### 1-1 Objective of the present study

Controlled crystal growth by molecular beam epitaxy (MBE) has paved a way to fabricating novel structures in nm-scale. While covalent chemical bonds exist at the interfaces fabricated by ordinary MBE, interfaces of layered materials are only connected with weak van der Waals forces. Recently-invented van der Waals epitaxy (VDWE) utilizes this property of layered materials and succeeded in fabricating hetero-interfaces with highly different lattice constants and physical properties. These interfaces can be called as "van der Waals interfaces" because it is considered that the two sides of the interface are connected by van der Waals forces.

In the present study, I have pursued two fundamental phenomena in solid state physics and chemistry by applying VDWE and surface science techniques. One is the charge density waves (CDWs) in metallic layered materials. CDW is a phase transition caused by Fermi-surface driven instability of low dimensional metals, which will be explained in section 1-3. The other phenomenon, structural polytypes, changes physical properties of the material as reviewed in section 1-4. The formation mechanism of the polytypes is not fully understood.

The objective of the present study is to understand and control these properties in ultrathin films fabricated by VDWE. Special attention was paid to the film / substrate interaction at the van der Waals interfaces. The measurement was performed with a variety of surface science techniques. The structures of the films were studied with electron diffraction, grazing incidence x-ray diffraction (GID) and scanning tunneling microscopy (STM). Electron spectroscopies, i.e. x-ray photoelectron spectroscopy (XPS) and electron energy loss spectroscopy (EELS) were fully utilized to investigate electronic structures of the grown films. The physical property of the films was measured in macroscopic electric conductivity measurement. Electronic properties of the

interfaces were investigated through the work function measurement of constituent layered materials and photoemission spectroscopy of heterojunctions.

The present thesis consists of 11 chapters which are summarized as follows.

Chapter 1 is the introduction, which explains the basic concepts used in the following parts. Chapter 2 is devoted to the description of experimental techniques and apparatus used in the present study. In chapter 3, work functions of layered metal chalcogenides are measured systematically for the first time. Work function is an important parameter which determines the electron transfer at surfaces and interfaces. The measured values are utilized in the following chapter for the study of the electronic properties of the interfaces. Epitaxial growth of $TaS_2$ and $TaSe_2$ by VDWE is reported in chapter 4. These are metallic layered materials known for noticeable CDW transitions. The controllability of the polytypes by the growth temperature and the choice of the substrates was discovered through the measurement of the characteristic peak shape of Ta(4f) core level spectra in photoemission. The polytypes of monolayer films were related to the work functions of the substrates. A new model of the formation of some polytypes - electrostatic energy at interface electronic dipole layers - is presented by using this knowledge. STM and electronic conductivity measurement suggest the occurrence of disturbed CDW in the grown film. Chapter 5 reports the three dimensional structure determination of films with nm thickness by grazing incidence x-ray diffraction (GID). GID is a new technique in surface science introduced with the advent of synchrotron radiation. It was found that the polytypes of $TaSe_2$ and $NbSe_2$ were dependent on growth temperature and substrate material. It provides information on the growth process of VDWE. Physical and chemical properties of van der Waals interfaces other than CDW are studied in Chapter 6. Metal-semiconductor interfaces consisting of semiconductor $SnSe_2$ and $WSe_2$ are fabricated by VDWE. It was found that $SnSe_2$ can be grown epitaxially at the

substrate temperature 230°C, which is the lowest record in VDWE of layered materials. Chapter 7 reports the study of surface and interfaces of $1T-TaS_2$ which is one of the most famous CDW materials. $SnSe_2$ and metals with FCC structures were epitaxially grown on $1T-TaS_2$ and their effects on CDW are investigated. In the above, x-ray photoemission spectroscopy is mainly used for the characterization of the films and interfaces. Electron energy loss spectroscopy (EELS) is another useful tool to investigate the electronic structure of interfaces, owing to the variable probing depth controlled by incident electron energy. In chapter 8, the relationship between incident energy and intensity in EELS is studied for the detailed understanding of this depth profiling procedure in EELS. The importance of the diffraction effect is reported. Chapter 9 and 10 deal with the instrumental aspect of VDWE. Chapter 9 describes the observation of the intensity oscillation of reflection high energy electron diffraction (RHEED). Chapter 10 reports the thermal decomposition of $SnS_2$ and $SnSe_2$ which are studied as candidates for novel S and Se sources.

### 1-2. Layered metal dichalcogenides and van der Waals epitaxy

Metal dichalcogenides ($MX_2$) form a family of layered materials which consists of more than 40 compounds [1]. The structures of a unit layer of $MX_2$ are shown in Fig. 1-2-1. The stacking of these layers is dependent on the crystals and called polytype (section 1-4). The $MX_2$ family includes materials with various lattice constants and physical properties as indicated in Table 1-2-2 [2]. This variety of physical properties is related with the electron count per M atom, which is dependent on the group in the periodic table. The schematic band structure is shown in Fig. 1-2-3 [1]. The above dependence is roughly explained by a rigid band scheme.

VDWE was first introduced as the epitaxy of these layered $MX_2$ [3]. When the elements M and X are evaporated in ultrahigh vacuum condition and deposited onto dangling-bond-free surfaces at appropriate temperature, epitaxial

films of $MX_2$ are formed on the substrate without severe constraints of lattice matching conditions. Although the detail of the mechanism is only speculative yet, it is accepted that the lack of strong chemical bond across the interface is essential to the good quality of the epitaxial films. The forces which combine the interface are usually mentioned as van der Waals forces, but the importance of electrostatic interaction is revealed in the present study (chapter 4).

## 1-3. Charge density wave (CDW)

Metallic $MX_2$ have been studied in detail in solid state physics as quasi two dimensional (2D) conductors. In many cases, low dimensional free electrons are subject to localization of carriers accompanied by periodic lattice distortions at low temperature. This is called Peierls transition and CDW in the cases of 1D and 2D, respectively. CDWs found among $MX_2$ are tabulated in Table 1-3-1. These CDWs are strongly dependent on the electronic structure of the materials, in particular, the shape of Fermi surface. Charge transfer associated with doping and intercalation transforms CDWs drastically [4].

In the present research, CDWs of $TaS_2$ and $TaSe_2$ films grown by VDWE were studied by various methods. CDWs of $TaS_2$ and $TaSe_2$ in the bulk materials are illustrated in Fig. 1-3-2 ~ 3. They are strongly dependent on the polytypes. Fig.1-3-2 shows the transition temperature and the type of periodic lattice distortions [5]. The structure of the CDW distortion is not necessarily commensurate with the basic lattice in the normal state and it is determined by the competition between Fermi surface nesting and the commensuration, which is dependent on the temperature. Electronic conductivity exhibits characteristic temperature dependence associated with the CDW transitions (Fig.1-3-3 [6]). It should be noted that the resistivity changes more than one order of magnitude in $1T\text{-}TaS_2$ and $1T\text{-}TaSe_2$.

Surface scientific approaches were applied to the CDW of $TaS_2$ and $TaSe_2$ before the present research. x-ray photoelectron spectroscopy [7] shows splitting of Ta(4f) core levels in 1T-type crystals caused by the commensuraiton of CDW. When CDW is commensurate with the lattice, the environment of Ta atoms is separated into three kinds, of which population ratio is 6: 6: 1. A 2H-type crystal does not show the splitting. This property of XPS is utilized in chapter 4.

Although CDWs basically arise from the two dimensional structure, the effect of confinement or interaction at the interface with other materials cannot be deduced *a priori*. The difference in the transition temperature in the octahedral layer of 1T and 4Hb polytypes is suggesting the need for the investigation of these effects. However, very few attempts have been made for the fabrication of thin films to see the size effect or interface effect of CDW. Only one report is found by the present author on the extrafoliation of $TaS_2$ after electrochemical intercalation of hydrogen [8], but no occurrence of CDW was reported. In the present study, interfaces of $TaS_2$ and $TaSe_2$ are studied in two ways: one is the fabrication of monolayer films of these materials, and the other is the epitaxial growth of different materials on these ones (Fig. 1-3-4). They are reported in chap 4 and 7, respectively.

## 1-4. Polytypes

Layered materials are frequently found in several different structures with nearly the same chemical stoichiometry. This phenomenon is called "polytypism" and the different structures are called "polytypes." According to [9], the earliest report of the polytype goes back to 1912 on SiC [10], while the first paper on the polytype of $MX_2$ was published in 1964 [11] for a mineral molybdenite ($MoS_2$). Polytypism in other $MX_2$ was discovered in the following 1960s and early 1970s. The structures of $MX_2$ are shown in Figure 1-4-1 ~ 3 [12]. Since the physical properties are sometimes strongly dependent on the polytypes as seen in the cases of CDW and superconductivity [13], considerable efforts to understand and control the polytypes have been made so far.

The "polytypism" can be classified as follows: (i) difference in the coordinations around the metal atom, which are called "octahedral" (OC) and "trigonal prismatic" (TP), and (ii) different combinations in the stacking of these OC or TP layers. There are many theories presented to explain the formation of the polytypes, but the discussion has not been settled yet. As for (i), many authors noticed a systematic trend with the electron count per metal atom, that follows the sequence of OC(group 4 and 5 metals) - TP (group 5 and 6 metals)- distorted OC (group 7 metals). This trend has been explained by [14] using total energy calculation. The van der Waals radii and ionicity of the metal and chalcogen also play important roles [15] as seen from the dependence on the period of the elements. The theories to explain (ii) are not satisfactory at present. There are several concepts to explain the difference in stacking. The earliest one was the spiral growth theory [16]. According to this theory, the number of unit layer per unit cell is determined by the period of the spiral in the growth. Although this theory is easy to understand, it cannot explain the materials dependence of the polytypes only by itself. Until now, several theories including energetical and statistical treatment [9], modeling of the growth process [17], and ordering of the stacking fault [9] appeared. It seems that the "order-disorder" theory by Palosz is the only one which treats the materials dependence to some extent. However, its application is limited to $CdI_2$ type crystals which consist only of OC layers, because the treatment becomes too complex and because too much arbitrary assumptions are needed for other kinds of polytypes. It is also reported that the polytypes are also dependent on stoichiometry [18].

With regard to the present study of van der Waals interfaces, two aspects of polytypes should be considered. One is the understanding of the mechanism of the polytypes. Since the growth parameters can be controlled more flexibly, VDWE will be effective in the study of the polytypism. The other is the physical property of the grown films. The polytypes change physical properties of the materials drastically. Superconductivity of $NbSe_2$ is only found in 2Ha and 4Ha, and CDWs of $TaS_2$ and $TaSe_2$ are dependent strongly on the polytypes. It is therefore important to know the polytypes of the grown materials in the study and the application of VDWE of layered materials. Nevertheless only a few surface science techniques can be applied to determine the polytypes of ultrathin films. One of the few successful technique was grazing incidence x-ray diffraction, which is reported in chapter 5.

## Octahedral (OC)  Trigonal Prismatic (TP)
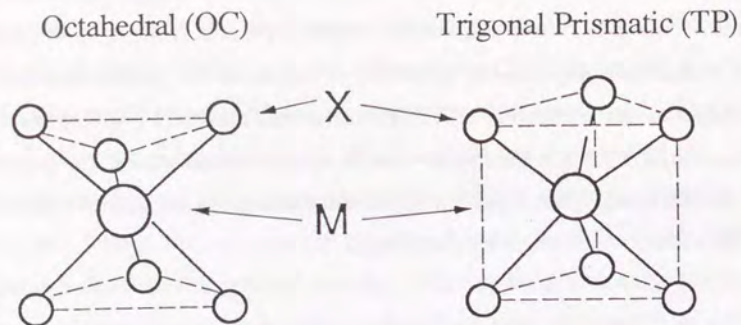


Fig. 1-2-1: Two types of the coordination of the metal in a unit layer of $MX_2$
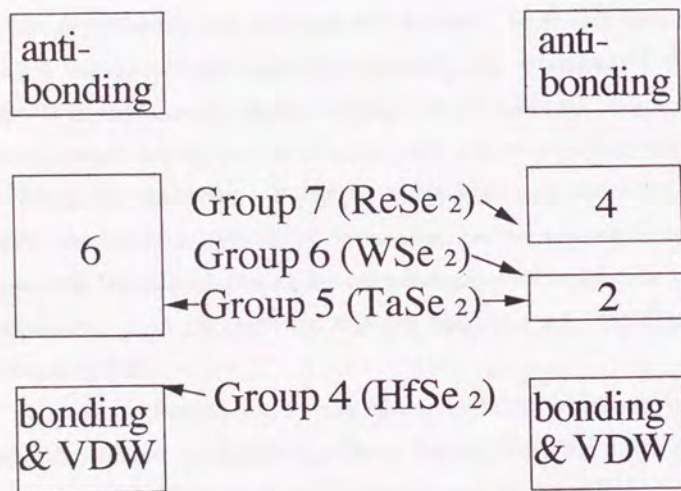


Fig. 1-2-3: Schematic band diagram of $MX_2$, obtained from a simple valence bond picture.[1]

| | lattice constants(Å) | electronic property (*) | band gap (eV) |
|---|---|---|---|
| **Group 4** | | | |
| $TiS_2$ | 3.4048 | S | i: 0.70 [2a], 0.23 [2b] |
| | | | d: 1.1t [2c], 0.84t [2b] |
| $TiSe_2$ | 3.535 | SM | i: -0.18t [2d];  d:0.35t [2d] |
| $ZrS_2$ | 3.662 | S | i: 1.68 [2e], 1.14t [2f] |
| $ZrSe_2$ | 3.770 | S | i: 1.20 [2a], 0.75t [2f] |
| $HfS_2$ | 3.635 | S | i: 1.96 [2e], 1.9t [2g] |
| $HfSe_2$ | 3.748 | S | i: 1.13 [2e],1.1t [2g] |
| **Group 5** | | | |
| $VSe_2$ | 3.35 | M | |
| $NbS_2$ | 3.31 | M | |
| $NbSe_2$ | 3.45 | M | |
| $TaS_2$ | 3.31/3.346 | M | |
| $TaSe_2$ | 3.436/3.477 | M | |
| **Group 6** | | | |
| $MoS_2$ | 3.160 | S | i: 1.23 [2j] |
| | | | d: 1.971e(2H,LNT) [2h], 1.89e(2H,RT) [2i] |
| $MoSe_2$ | 3.288 | S | d: 1.69e(2H,LNT) [2k]; i: 1.09 [2j] |
| $\alpha$-$MoTe_2$ | 3.517 | S | i: 0.9 [2j] |
| $WS_2$ | 3.154 | S | i: 1.35 [2j]; d: 1.75 [2j] |
| $WSe_2$ | 3.286 | S | d: 1.782e (2H,117K) [2l] |
| **Group 14** | | | |
| $SnS_2$ | 3.639 | S | i: 2.21a [2d], 2.22a [2a], 2.07f [2m] |
| | | | 2.14e(E // c,300K)[2q], |
| | | | 2.25e(E⊥c,300K)[2q] |
| | | | d: 2.88f [2m] |
| $SnSe_2$ | 3.811 | S | i: 1.03f [2m], 1.0f [2n,2o,2p], |
| | | | 0.97 [2m], 1.1 [2a] |
| | | | d: 1.97a (LNT) [2m], 1.62f [2m] |

* S: semiconductor, M: metal, SM: semimetal
d: direct;  i: indirect;  a: allowed;  f: forbidden
LNT: 77K.  RT: room temperature
t: theoretical
e: derived from extrapolation of exciton sequence
[]: reference number

Table 1-2-2:  In-plane lattice constants [2p, 2r] and electronic and optical properties [2s,2t] of some $MX_2$'s.

Fig. 1-3-1: CDWs of MX$_2$

| material | periodic lattice distortion (a x a x c) | transition temperature |
|---|---|---|
| 1T-TiSe$_2$ | 2 x 2 x 2 | 202K |
| 1T-VSe$_2$ | 4 x 4 x ~3 | ~110K |
| 2Ha-NbSe$_2$ | ~3 x 3 | ~33K |
| TaS$_2$ | see Fig. 1-3-2 | |
| TaSe$_2$ | | |

**TaS$_2$**

Ref.5

| | | |
|---|---|---|
| 1T | C($\sqrt{13}\times\sqrt{13}$) $\xleftarrow{195K}$ NC $\xleftarrow{350K}$ I $\xrightarrow{220K}$ | |
| 2Ha | C(3x3) $\xleftrightarrow{80K}$ Normal | |
| 4Hb | OC layer | C($\sqrt{13}\times\sqrt{13}$) $\xleftrightarrow{315K}$ I |
| | TP layer | C(3x3) $\xleftrightarrow{20K}$ Normal |

**TaSe$_2$**

Ref. 4

| | | |
|---|---|---|
| 1T | C($\sqrt{13}\times\sqrt{13}$) $\xleftrightarrow{473K}$ I | |
| 2Ha | C(3x3) $\xleftrightarrow{120K}$ Normal | |
| 4Hb | OC layer | C($\sqrt{13}\times\sqrt{13}$) $\xleftrightarrow{410K}$ I |
| | TP layer | C(3x3) $\xleftrightarrow{75K}$ Normal |

Fig. 1-3-2: CDWs of TaS$_2$ and TaSe$_2$

13
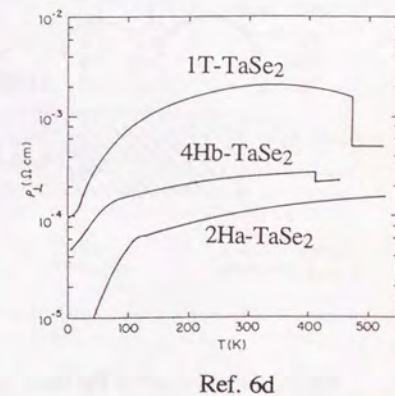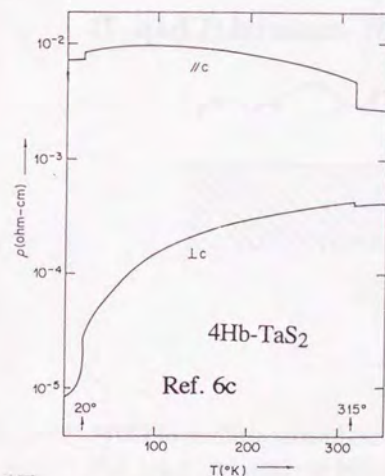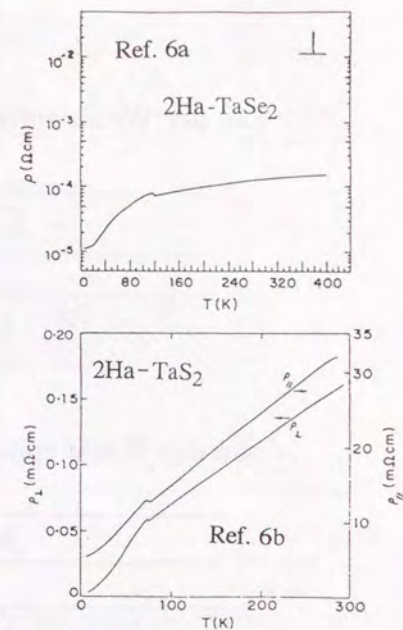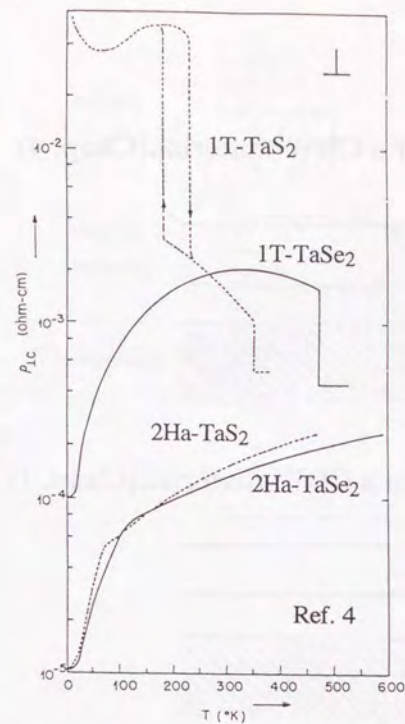


Fig. 1-3-3: Temperature dependence of electric resistivity of bulk TaS$_2$ and TaSe$_2$

// and ⊥ denote the direction of the electric current parallel and normal to the c-axis perpendicular to the layers, respectively.

14

## van der Waals epitaxy of a CDW-material.(Chap. 4)

CDW

////// MX₂ //////
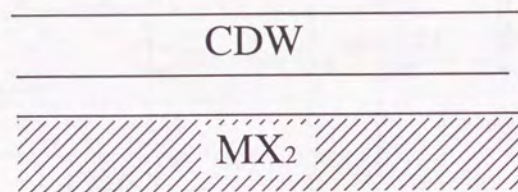
## van der Waals epitaxy on a CDW-material.(Chap. 7)

MX₂

////// CDW //////
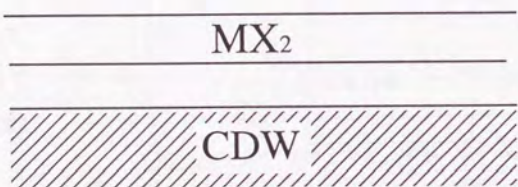
## Metal deposition on a CDW-material.(Chap. 7)

metal

////// CDW //////

Fig. 1-3-4:  Tactics for the study of size and interface effects of CDW.
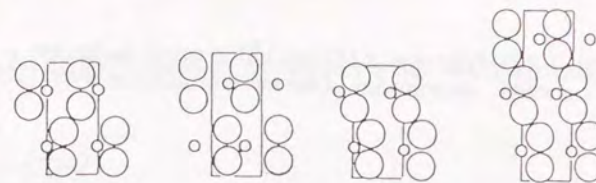
| structure | | | | |
|---|---|---|---|---|
| polytype | 2Ha | 2H | 2Hb | 3R |
| symmetry | $P6_3/mmc$ | $P6_3/mmc$ | $P\bar{6}m2$ | $R3m$ |
| compounds | $TaS_2$ $TaSe_2$ $NbS_2$ $NbSe_2$ $NbSSe$ $NbSTe$ | $TaSe_2$ $NbSe_2$ $MoS_2$ $MoSe_2$ $MoTe_2$ $WS_2$ $WSe_2$ | $TaSe_2$ | $TaS_2$ $TaSe_2$ $NbS_2$ $NbSe_2$ $MoS_2$ $MoSe_2$ $WS_2$ $Nb_{1+x}S_2$ for $x \leqslant 0.29$ $TaS_{2-x}Se_x$ for $x \geqslant 0.4$ |



| 4Ha | 4Hc | 6R |
|---|---|---|
| $P\bar{6}m2$ | $P3m1$ | $R3m$ |
| $TaSe_2$ $NbSe_2$ | $TaS_2$ $TaSe_2$ $TaS_{2-x}Se_x$ for $x \geqslant 0.8$ | $Ta_{1+x}S_2$ ● = extra Ta-atom between the layers |

Fig. 1-4-1:  Polytypes of MX₂ (11$\bar{2}$0 sections) having a  trigonal prismatic  coordination of the metal atom in the layer.  [12]

Fig. 1-4-2: Polytypes of MX$_2$ (11$\bar{2}$0 sections) having an octahedral coordination of the metal atom in the layer. [12]



| structure | | | | |
|---|---|---|---|---|
| polytype | 1T | 2H″ | 3R | 6R |
| symmetry | P$\bar{3}$m1 | P6$_3$/mmc | R3m | R3m |
| compounds | TaS$_2$ | TaS$_2$ | TaS$_2$ | TaS$_2$ |
|  | TaSe$_2$ | TaSe$_2$ | TaSe$_2$ | |
|  | NbSe$_2$ | | Ta$_{1+x}$S$_2$ | |
|  | TaS$_{2-x}$Se$_x$ | | | |
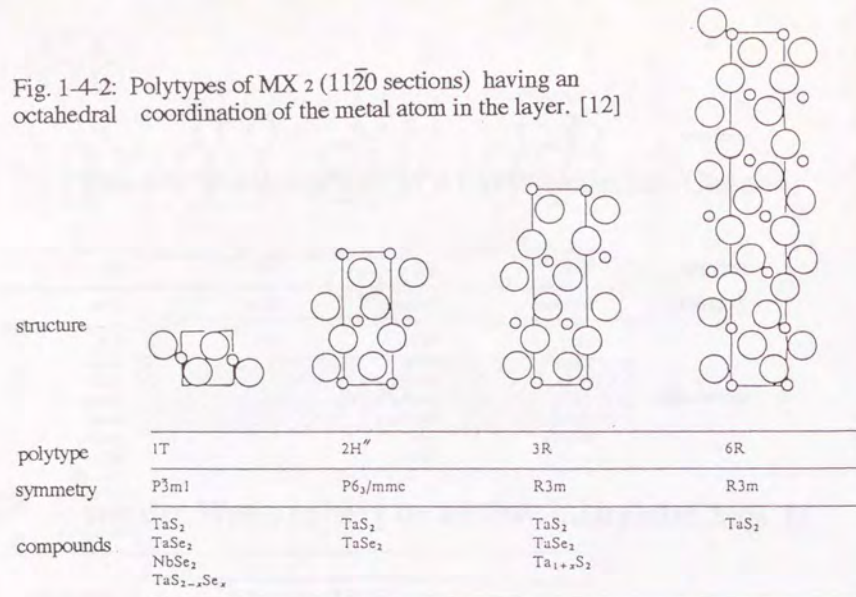
Fig. 1-4-3: Polytypes of MX$_2$ (11$\bar{2}$0 sections) having both of the trigonal prismatic and octahedral coordination of the metal atom. [12]



| structure | | | | |
|---|---|---|---|---|
| polytype | 4Hb | 4Hd$_I$ | 4Hd$_{II}$ | 6R |
| symmetry | P6$_3$/mmc | P3m1 | P$\bar{6}$m2 | R3m |
| compounds | TaS$_2$ | NbSe$_2$ | NbSe$_2$ | TaS$_2$ |
|  | TaSe$_2$ | | | TaSe$_2$ |
|  | TaS$_{2-x}$Se$_x$ | | | |
|  | $0.2 \leqslant x \leqslant 0.4$ | | | |
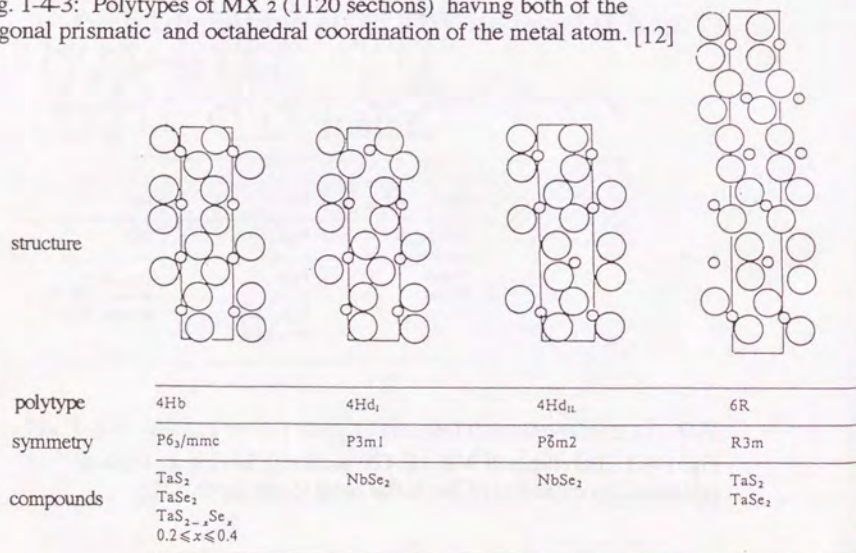
# Chapter 2. Experimental methods and instruments

Experimental methods and instruments are described in this chapter. Section 2-1 is the illustration of the vacuum system, followed by the explanation of evaporation sources in section 2-2. Section 2-3 and 2-4 describe the diffraction technique and electron spectroscopy for analyzing the structure and electronic structure of films and substrates. Section 2-5 describes the principle of scanning tunneling microscopy (STM). In section 2-6, the low temperature measurement systems are introduced.

## 2-1. Vacuum system

VDWE and characterization by XPS (x-ray photoelectron spectroscopy) , LEED (low energy electron diffraction), EELS (electron energy loss spectroscopy) and AES(Auger electron spectroscopy) were performed in ultrahigh vacuum chambers pumped separately and connected with gate valves. Although the experiments were performed in different systems during the three years of the present research, the structures of them are nearly the same, as illustrated in Fig. 2-1-1. The growth chamber had a base pressure of $1 \times 10^{-7}$ Pa and equipped with evaporation sources, a sample stage with heater, and a reflection high energy electron diffraction (RHEED) apparatus. The analysis chamber, which had a base pressure of the order of $10^{-8}$ Pa, was equipped with a sample stage using liquid $N_2$ cooling and electric heating (Fig. 2-1-2). The lowest temperature obtained in the in-situ measurement system was about 150K. The analysis chamber was equipped with one or two of XPS, EELS, LEED, and AES at a time.

The $MX_2$ substrates were cleaved with adhesive tapes in the vacuum better than $1 \times 10^{-5}$ Pa, and sometimes in the ultrahigh vacuum ($<10^{-7}$ Pa) in the analysis chamber when their surfaces were easily contaminated by the residual gas. HOPG substrates were cleaved in air and cleaned by heating in the growth chamber at 800°C.

## 2-2. Evaporation sources

All elements for the growth were evaporated from heated elemental substances. Se was evaporated from a Knudsen cell illustrated in Fig. 2-2-1. Since the sublimation temperature (~120°C) is much lower than the temperature for the bake-out of vacuum systems (~200°C), a load lock mechanism was necessary. S source was constructed in the similar form, but special attention in the operation was needed due to the high vapor pressure of S. Since evaporated sulfur stuck to the wall of the sources and the blades of the turbo molecular pumps, frequent overhaul, i.e., washing in boiling glycerin was necessary. It was found that the vapor pressure at room temperature was enough to produce the S beam flux of $10^{-6} \sim 10^{-5}$ Pa at the substrate position when the valve to the differential pump was closed. Since these sources are inconvenient for operation, the decomposition of $SnS_2$ and $SnSe_2$ are studied in chapter 9. Nb and Ta was evaporated from electron bombardment sources or from Joule heated wire of the elements (Fig. 2-2-2). The former ones utilized the electron bombardment with electrostatic or magnetic deflection and were useful to make thick films with more than 10ML thickness. The latter used the heating of 0.5mmφ wire with direct current of about 20 A. This source has a convenience for construction and sufficient to make the films not thicker than 10ML. Sn was evaporated from the melt heated by contact with a Mo heater, or from electron bombardment sources.

## 2-3. Structure analysis by diffraction

Electron diffraction techniques i.e., reflection high energy electron diffraction (RHEED) and low energy electron diffraction (LEED) were used in the present research for the in-situ structure analysis of grown films. The principles of these techniques are illustrated in Fig. 2-3-1. By RHEED and LEED it is possible to obtain information on the atomic arrangement in the surface plane. Grazing incidence x-ray diffraction, used for the structure analysis for the direction normal to the surface, is described in detail in chapter 5.

## 2-4. Measurement of electronic structures

Electronic structures of the substances are measured by electron spectroscopies, XPS, EELS and UPS. XPS and UPS utilize the photoelectron emission which occurs when photons are irradiated to the sample surface (Fig. 2-4-1). It should be noted that the binding energy of electrons in the solid is

measured relative to the Fermi level. This property of photoemission is utilized in the measurement of work functions (chapter 3). In AES, kinetic energy of electrons emitted by Auger effect is measured as shown in Fig. 2-4-2. The characteristic peak shape of Cu in AES was used for the determination of ionic state of Cu intercalated in $1T\text{-}TaS_2$ in chapter 7. The detail of the principle of EELS is provided in chapter 8.

## 2-5. Scanning tunneling microscopy (STM)

STM utilizes the tunneling of electrons between a sample surface and a probing tip with one atom on the top of it. The position of the tip is controlled by three dimensional piezoelectric positioner with sub Å resolution. A commercial STM Nanoscope II (Digital Instruments) with W-tips was used in the present experiment. The measurement was performed at room temperature in the ambient atmosphere.

## 2-6. Low temperature measurement

Electric conductivity of the grown films was measured at low temperature down to 0.45K. Two different cryostats were used to ensure the accuracy of the temperature measurement. The temperature above 1.87K was produced in the $^4$He cryostat of Magnetic Property Measurement System (MPMS: Quantum Design). The temperature was controlled by pumping of liquid $^4$He and heating of $^4$He gas in the sample space. The accuracy of the temperature was ±0.5% from 1.87K to 100K and ±1% from 100K to 300K. In order to measure the temperature dependence automatically, MPMS controller was interfaced with resistivity measurement system.

The temperature below 1.87K was achieved by using a $^3$He cryostat. This cooling system was constructed and operated in cooperation with Prof. Suematsu's group in Department of Physics. The cooling system and the gas handling pipelines are illustrated in Fig. 2-6-1 and -2, respectively. The temperature was estimated from the pressure of $^3$He gas, which was nearly in equilibrium with liquid $^3$He, measured with a diaphragm-type gauge.

heater

sample

liq.N2

RHEED

shutter

S  Ta  Se
Nb

XPS

LEED

UPS
EELS

Entry
chamber

Analysis
chamber

Growth chamber
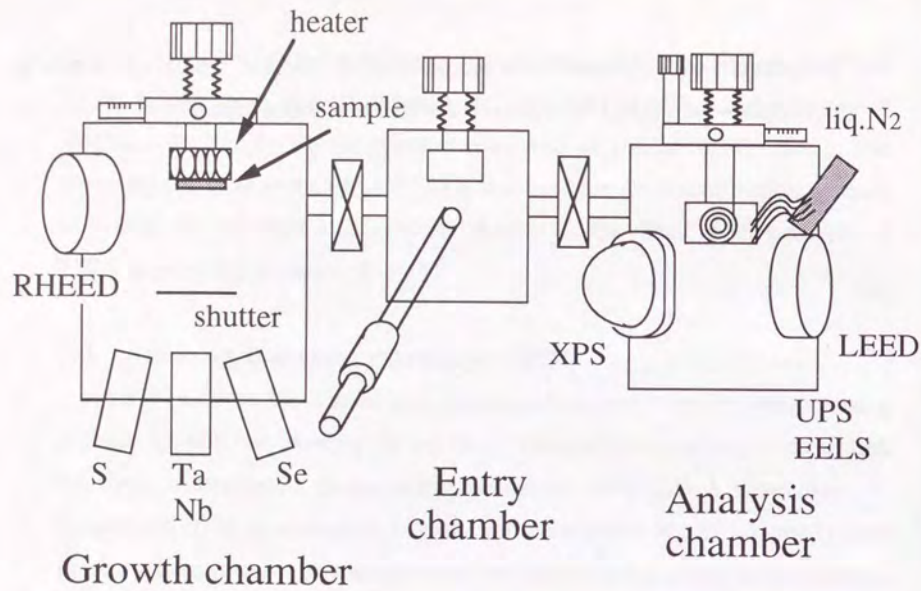
Fig. 2-1-1: Schematic diagram of vacuum System.

Mo block

specimen

liq.N2

spring and screw to
make thermal contact

heater

thermo
couple

Cu rope
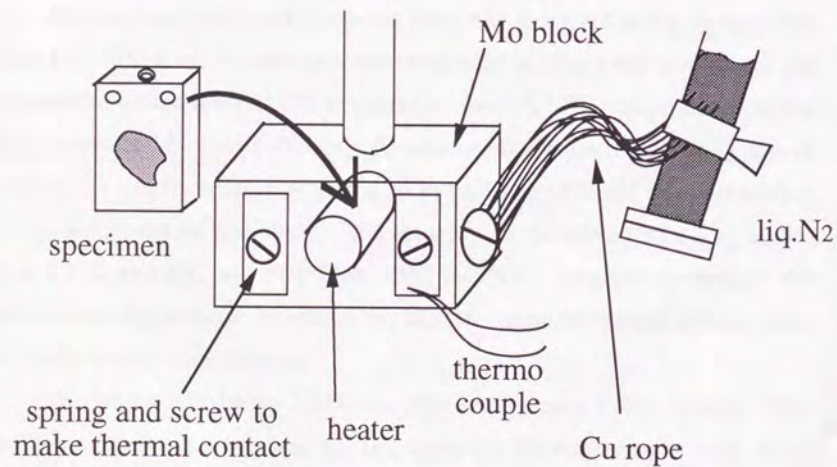
Fig. 2-1-2: Specimen holder of the Analysis chamber

**Growth
chamber**

Se, S

pump

heater
(Ta)

thermo
couple

heater &
thermo
couple

Fig. 2-2-1: S and Se source

## Left page (25)

Ta, Nb

$e^-$

crucible (graphite)

magnet

water cooling

10V

"E-gun" : an electron bombardment source

3~10kV

Ta wire souce

Ta 1mm$\phi$ x 4

Ta 0.5mm$\phi$

Ta
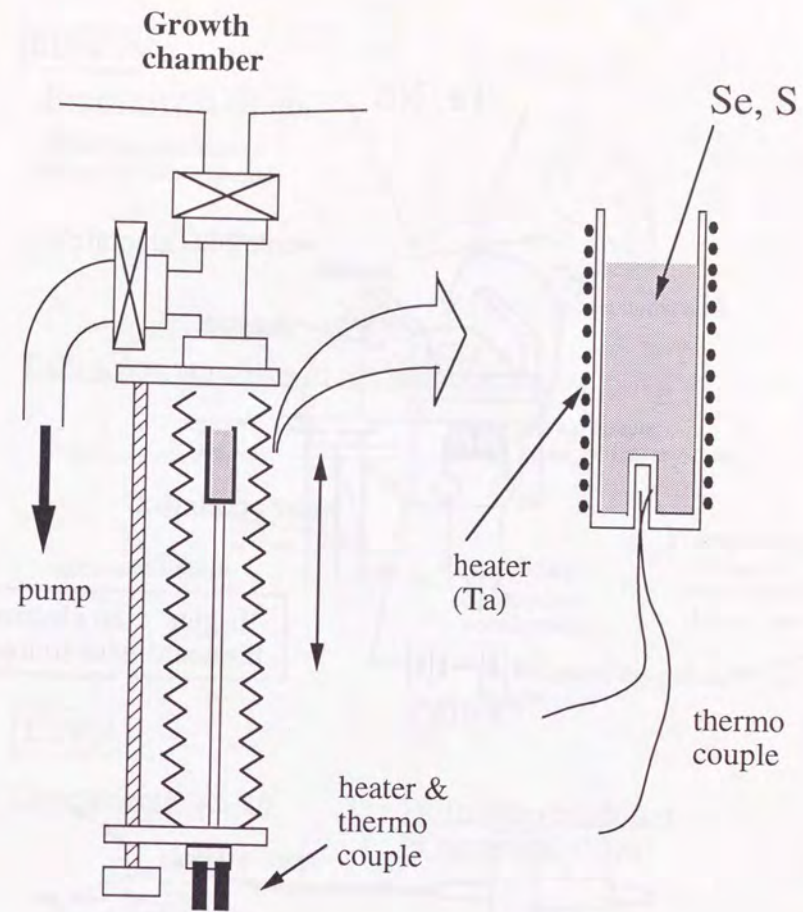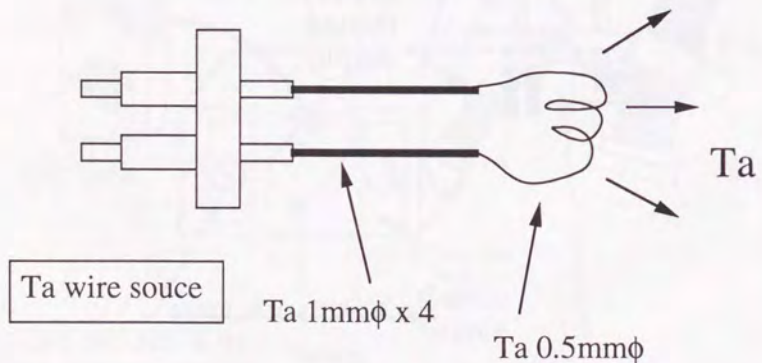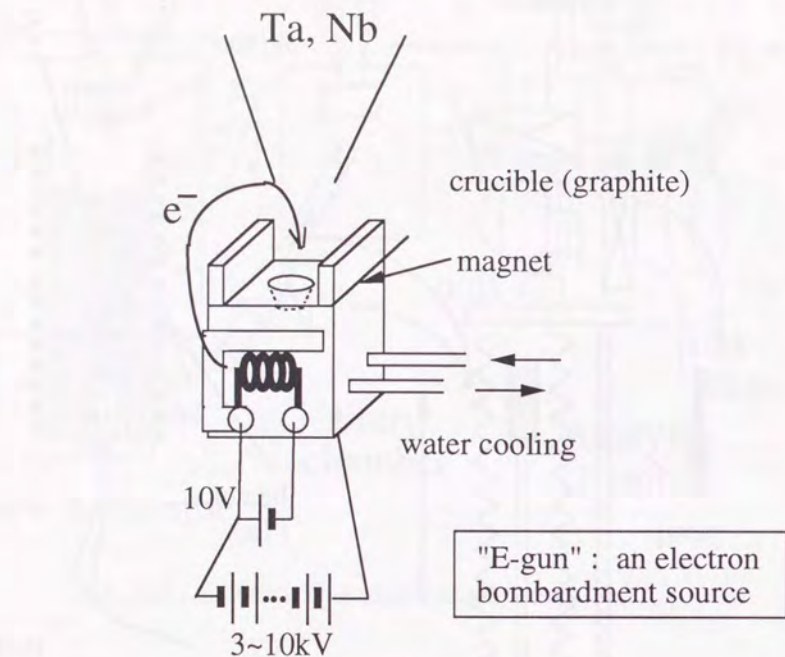
Fig. 2-2-2: Metal evaporation sources.

25

## Right page (26)

RHEED

### Experimental set-up

~20kV incident energy
below ~1° incident angle
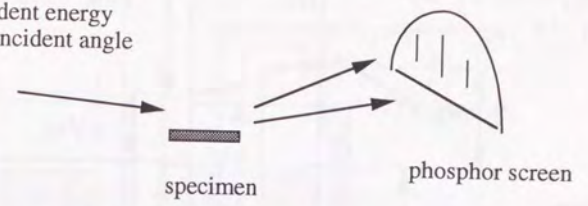
specimen

phosphor screen

### Diffraction condition in reciprocal space

Ewald sphere
(energy conservation)

incident electron

$k_{in}$

specimen surface plane

Bragg rods
(momentum conservation)

elongated spots /
streaks on
concentric circles
(Laue zone)

dependent on the surface
morphology

LEED

### Experimental set-up

phosphor screen

e-gun

specimen

50~300eV
normal incidence

### Diffraction condition in reciprocal space

$k_{in}$

Ewald sphere

Bragg rods
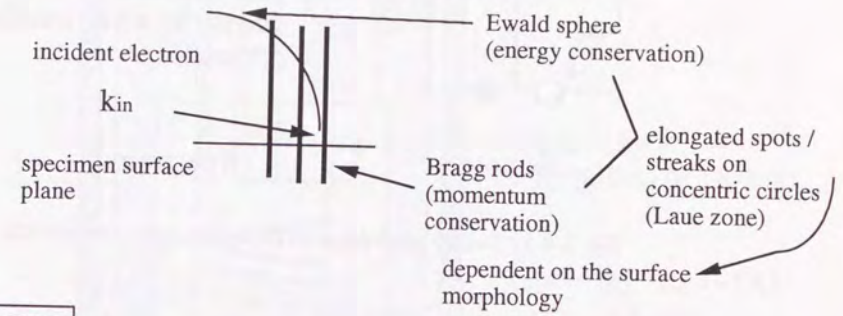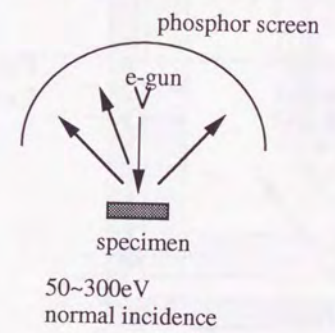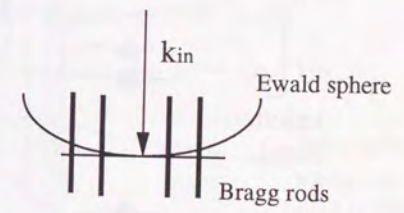
-> spot patterns related with
the symmetry of the crystal

The dependence on $k_{in}$ reflects three dimensional structure of the surface.

Fig. 2-3-1:  Principles of RHEED and LEED

26

$h\nu$  $E_{kin}$

$e\Phi$

$eV_{SP}$

Fermi Level

$E_B$

Electric field
due to the workfunction
difference

Sample                    Spectrometer
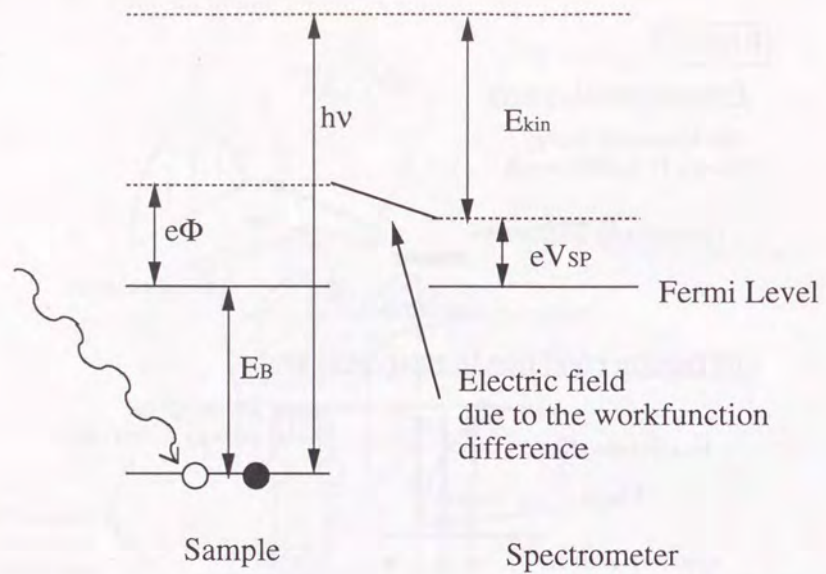
Fig. 2-4-1: Energy level diagram for a photoemission process



$e^-$

$E_{kin}$   vacuum
level

Fermi
Level

valence
band

$L_3$ (2p$_{3/2}$)

Initial          Core hole          Auger
state         production         process
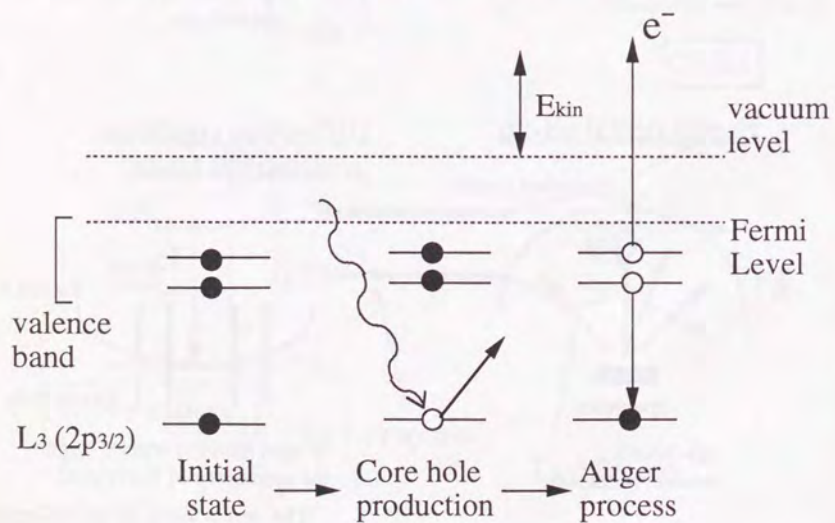
Fig. 2-4-2: Energy level diagram for an L₃VV Auger process.
$E_{kin}$ is measured in Auger electron spectroscopy.

pump

closed pumping
gas $^3$He return

pump

gas $^3$He
(liquified in 1K-pot)

liq.$^4$He (~1K)
"1K-pot"

liq.$^4$He(4.2K)

liq. N₂

liq.$^3$He

insuration
vacuum
(~ $10^{-4}$Pa)

sample
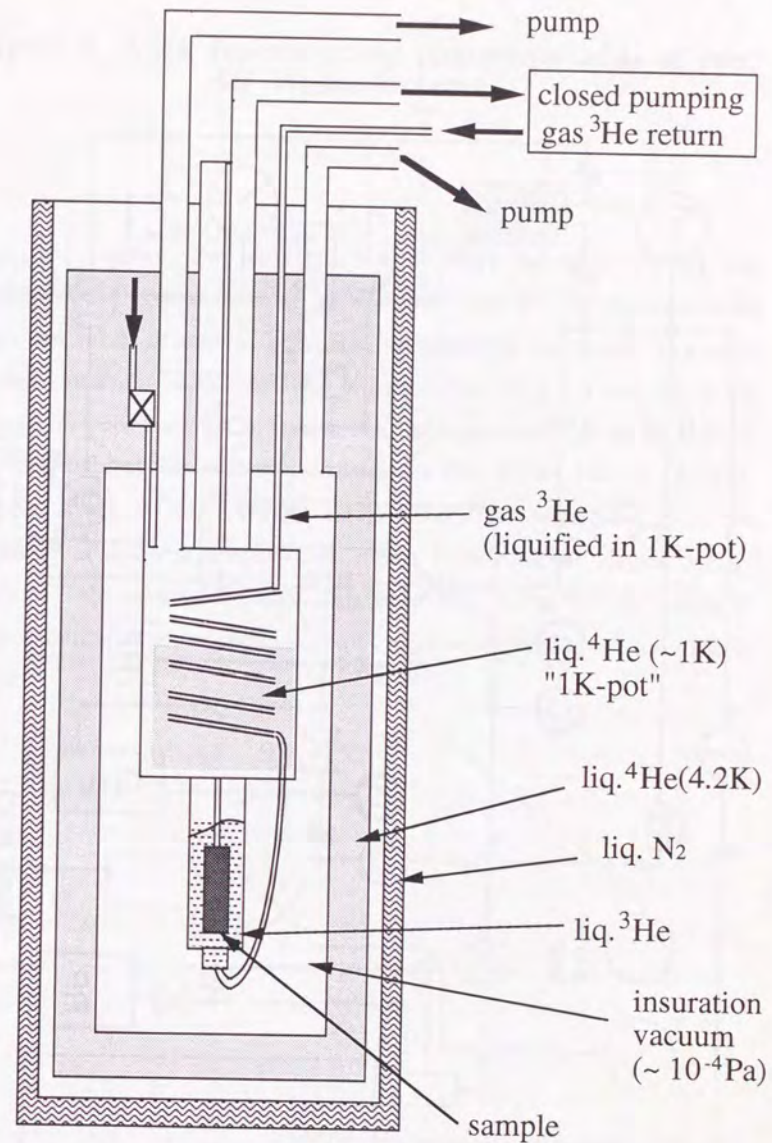
Fig. 2-6-1: $^3$He cryostat
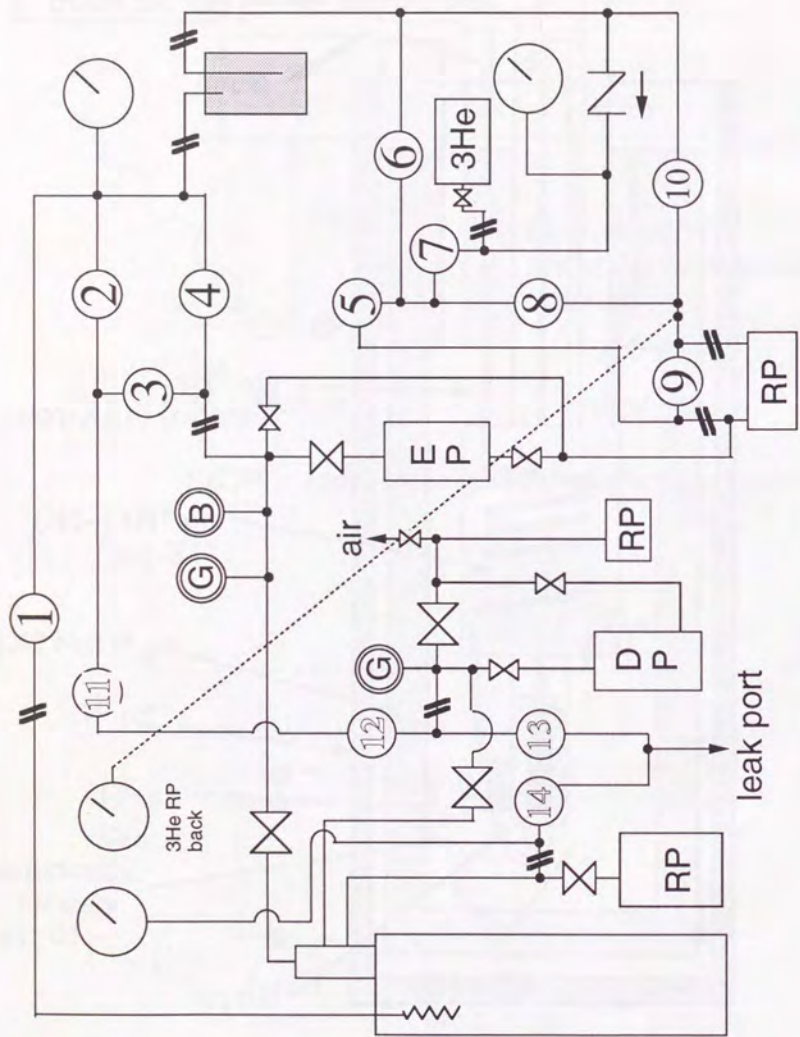
Fig. 2-6-2: Gas handling system for $^3$He cyostat

# Chapter 3. Work functions and photothresholds of van der Waals surfaces

In this chapter, the measurements of work functions (WFs) and photothresholds of layered materials are reported. The WF and photothreshold are important values of surfaces when electron transfer is concerned. In section 3-1, an introduction of work function is provided. Section 3-2 is a review of the methods to measure the WF. In section 3-3, the experiment and the analysis of WFs and photothresholds of layered materials ($ZrSe_2$, $HfSe_2$, $NbSe_2$, $1T-TaS_2$, $2Ha-TaS_2$, $MoS_2$, $MoSe_2$, $MoTe_2$, $SnS_2$, $SnSe_2$) are described. From the measurement at different temperatures, it was found that the charge density waves of $1T-TaS_2$ have exhibited no observable effect on the WF. In section 3-4, the possibility of the measurement of "local work functions" by STM is discussed.

## 3-1. Work function

### 3-1-1 Definition of the work function and photothreshold

Work functions (WFs) are important physical parameters to characterize surface properties, such as electron emission from materials and charge transfer at interfaces. The definition of the work function is the minimum energy to take one electron from the interior of a solid surface to some place far enough that the dynamic effects (e.g. image forces) from the surface is negligible (Fig. 3-1-1). Let $E(N)$ the energy of the ground state of a surface containing N electrons, then the work function $\Phi$ is written as

$$e\Phi = -E(N+1) + \{E(N) + V(\infty)\}$$
$$= -\partial E/\partial N + V(\infty) = -\mu + V(\infty), \qquad (3\text{-}1\text{-}1)$$

where $\mu$ is the chemical potential, $V(\infty)$ is the energy of the electron which has been extracted from the surface [1b]. It should be noted that the work function is referred with the index of the measured faces, since the potential energy $V(\infty)$ is dependent on the index of the surfaces even for the same material. This comes from the fact that the extracted electron remains near the surface in the ordinary measurement and application. The definition described above is adopted from the very early stage of the surface science [1]. In this sense, the energy to take a electron to a place of infinite distance is called "total work function" [1] . Besides the work function, there is an important quantity for semiconductors, a photothreshold. This value is defined as the minimum energy required to remove a valence electron from the interior of a solid surface.

### 3-1-2 Work functions of metals

Two factors are important to account for the WF of metals, i.e., many-body effect inside the bulk ('bulk' or 'chemical' term) and electric dipole layer at the surface ('surface' or 'electric' term). The former is explained as follows. There is a cloud of plus charges, or the region of electron deficiency, around an electron inside a solid. This plus charge arises from the repulsion of electron

mainly due to the Pauli's exclusion principle and the Coulomb repulsion, for the electron with the same and opposite spins, respectively. This electron deficiency region is called a "Fermi hole." When one electron is taken out from the solid, the electron is retracted by this Fermi hole and thus a part of WF is produced. It should be noted that this mechanism works also for the non-metallic materials although the properties of the potential is different.

For the latter "surface term", electric dipole layer caused by the tunneling of the free electrons from the surface is important. The material is suddenly cut at the surface and plus charges of ionic core does not exist outside. However, free electron tunnels into the vacuum for 1~10Å, which creates an electronic dipole layer. Kohn and Lang calculated the work function for various electron density by using jellium model, and obtained a good agreement with the experimental values of work functions [2]. When the electron density is increased, the surface term increases and the bulk term decreases. These terms nearly compensate each other and yield a smooth increasing function of the electron density. The difference of the work function by the surface indexes are explained by the change in the density of the ionic cores [2]. The result is that WF is an increasing function of the density of atoms at the surface. This theory also agrees with the experiments quantitatively [2] .

### 3-1-3 Work functions of non-metallic materials

Non-metallic materials have complications which do not exist in the metals. The effect of electric dipole potential caused by the electron tunneling ('surface' term) is negligible when the electron density is smaller than $\sim 10^{-20}$ cm$^{-3}$ [2]. In this case, the position of valence band maximum measured from the vacuum level, which equals to the photothreshold, is determined only by Fermi holes. In contrast to this simplicity of photothreshold, WF of semiconductors have not been examined in detail, since Fermi level of the material is strongly influenced by the dopants and the condition of the surfaces. In conventional materials like

Si and GaAs, these properties are strongly influenced by surface dangling bonds or surface recombination. Chemically saturated surfaces of layered materials are of particular interest in this sense because we do not need to consider such complications.

For insulators and nearly insulating semiconductors, the charging-up of the surfaces often occurs making the definition and the measurement of the WF difficult.

### 3-2. Methods to measure the work functions

*3-2-1 Measurement of WF*

WF is the energy to take an electron at Fermi level from the solid surface. The methods for the measurement are basically divided into two groups: direct and relative methods. The direct methods, which utilize the <u>real</u> electron emission from the surface, can measure the value of WF without any reference. On the other hand, the relative methods measure the contact potential difference which arises when the sample and the reference is connected. Here the WF of the reference must be known in advance. In contrast to the ionization potential of the atoms and molecules, the non-adiabatic nature of the direct method has negligible effect on the measured value. In solids, especially in conductive and semiconductive ones, electrons compensate the plus charge created by the electron emission. This process occurs quickly enough to ensure the equivalence of the measured value and the thermodynamic definition of WF. The basis of the above explanation is one-electron approximation in the solid state physics (e.g. band structure). The study of the electronic structure by photoemission will be impossible otherwise. On the other hand, the electron transfer is very slow in insulators, resulting in the charging-up of the samples which is easily detected.

*3-2-2 Photoelectron yield method*

This method measures the photoelectron yield as a function of photon energy. Basically, the photoelectron is emitted by the irradiation of photons which have the energy larger than the WF of the surface. In order to make a correction on the temperature of the sample, the photon energy is scanned near the threshold and the data are fitted to the Fowler's function (Fowler-plot):

$$J = \frac{4\pi meQ}{h^3} \int_0^{-\infty} t \ (e^{\frac{t-h\nu-e\Phi}{kT}} +1)^{-1} dt \qquad (3\text{-}2\text{-}1)$$

where J, Q, T and $h\nu$ are the photoelectron yield, apparatus constant, temperature and photon energy, respectively. The merit of this method is that the number of the data points can be increased at will and thus it is highly accurate.

*3-2-3 Thermal electron yield method*

The electrons in the metal is inside the potential barrier $e\Phi$ from the vacuum. When the temperature of the metal is raised, the energy of the electrons is increased and some electrons have enough energy to exit from the surface. This phenomenon is known as thermionic emission and the emission current density J follows Richardson-Dashman equation:

$$J = AT^2 e^{-\frac{e\Phi}{kT}} \qquad [A/m^2], \qquad (3\text{-}2\text{-}2)$$

where $A = 4\pi mek^2/h^3 \approx 1.2 \times 10^6$ A/m$^2$K$^2$ is the Richardson constant. A plot of log $J/T^2$ versus $1/T$ (Richardson plot) gives a line, and the WF, $\Phi$, is obtained from the trend of the line. This method is directly related with the application in a thermal electron gun, but it cannot be used to the materials which decompose at high temperatures (must be stable at ~1000K). In the practical measurement, a static potential is applied to the sample for the collection of the electron and the removal of the space charges near the surface. This causes the Schottky effect,

which lowers the apparent value of WF by $\Delta\Phi = -\sqrt{e^3|F|}$, where F is the electric field at the sample surface caused by the applied voltage.

### 3-2-4 Field emission method

When a strong electric field (>0.5V/Å) is applied to the metal surface, the thickness of the potential barrier for the electron near the Fermi level becomes small enough for the tunneling (~10Å). By using Wentzel-Kramers-Brillouin (WKB) approximation and neglecting the effect of image potential, emission yield J is given as :

$$ J \approx \frac{e^2 F^2}{8\pi h F} e^{-\frac{2\sqrt{2m}}{3e\pi hF} F^{3/2}}, \qquad (3\text{-}2\text{-}3) $$

where F is the electric field.

This is Fowler-Nordheim equation, and the WF is derived by applying high voltage (V) to a metal tip and measuring J as a function of V. F is usually assumed as $F \approx V/5r$ where r is the curvature of the tip. This method is only applicable to the metals, but it can be combined with the field electron / ion microscopy (FEM / FIM). This facilitates the measurement of WF for surfaces with different indexes. In relation to this method, the application of scanning tunneling microscopy is recently discussed [1c], which is reviewed in the appendix of this chapter.

### 3-2-5 Kelvin method

This method utilizes the contact potential difference. Let the two different metals be put aside to make a parallel plate capacitor and connect the plate with a wire via a sensitive current meter and a variable voltage source. If the difference of the work functions of two plates is not compensated by the applied voltage of the voltage source, then current is detected when the distance of the two plates is varied. Usually one plate is moved oscillatory and the current is amplified with a frequency-sensitive lock-in-amplifier. The merit of this method is that the vacuum condition is not necessary and that it thus can be used in various chemical atmosphere. The demerit of this method is that WF of one of the electrode must be known in advance.

### 3-2-6 Secondary electron threshold

This method was utilized in the present study to measure the WFs and the photothresholds of the layered materials. When light of energy hv is irradiated to the surface, photoelectrons are emitted (Fig. 3-2-1). Some of the electrons are inelastically scattered before exiting from the surface and lose most of their kinetic energy. These electrons are called "secondary electrons". The secondary electrons with lowest kinetic energy detected should have had the energy higher than Fermi level by the WF (eΦ) when they are in the solid, because otherwise the electron cannot go through the barrier. On the other hand, the photoelectrons with the highest energy had the energy hv inside the solid if the sample is metallic. Therefore by measuring the maximum ($E_{max}$) and the minimum energy ($E_{min}$) in the photoemission spectroscopy, WF is given by

$$ e\Phi = hv - (E_{max} - E_{min}). \qquad (3\text{-}2\text{-}4) $$

This method can be utilized to the non-metallic samples once $k_{max}$ for a metallic reference is measured, because the kinetic energy corresponding to the Fermi energy of the sample is determined only by the spectrometer set-up. The merit of this method is that the photothreshold and the photoelectron spectrum is obtained at the same time. The photothreshold, eΘ, is obtained from the binding energy for the top of the valence band ($E_v$) as:

$$ e\Theta = e\Phi + E_v. \qquad (3\text{-}2\text{-}5) $$

The demerit of this method is that (i) an expensive electron energy analyzer is needed, and that (ii) the applied static voltage causes refraction of electrons which leads to the broadening of the threshold and the inaccuracy of the measurement. This disadvantage (ii) of the method can be circumvented by

angle resolving the electrons to detect only the electron emitting perpendicular to the surface.

## 3-3. Work functions and photothresholds of layered metal chalcogenides

### 3-3-1 Introduction

As reviewed in the previous sections, WFs are important in the study of the charge transfer at interfaces. In addition to the importance in the present study, the measurement of WFs of the layered materials has another significance because the dangling bond free surfaces of $MX_2$ are also ideal substrates to observe molecules by scanning tunneling microscopy study [3]. Therefore, I have measured WFs and photothresholds of various layered metal dichalcogenides ($ZrSe_2$, $HfSe_2$, $NbSe_2$, $1T\text{-}TaS_2$, $2Ha\text{-}TaS_2$, $MoS_2$, $MoSe_2$, $MoTe_2$, $SnS_2$, $SnSe_2$). Although the WFs of some of the layered semiconductors have been measured in relation to the photo- and photochemical- electrocells made of layered semiconductors [4], those of metallic ones have not been measured yet.

There are two types of coordination around metal atoms as distinguished by 1T and 2Ha for octahedral and for trigonal prismatic coordination, respectively. Their structures are shown in Fig. 1-2-1. $1T\text{-}TaS_2$ is known for charge density waves (CDW), where the $\sqrt{13} \times \sqrt{13}$ superstructure appears below 600K due to charge density modulation [5]. Since the amplitude and the structure of charge density modulation vary with temperature, we also studied the temperature dependence of WF for $1T\text{-}TaS_2$. The photothresholds from the present experiment are compared with band calculations found in literature.

### 3-3-2 Experimental

The measurement was performed by using the secondary electron cut-off in ultraviolet photoelectron emission. The advantage of this method is that both work function and photothreshold are measured simultaneously [6]. We have utilized ARIES HAC-300 (VSW) angle resolved electron energy analyzer with a He-I discharge lamp (photon energy $h\nu=21.2eV$). A bias voltage ($E_A$) was applied to the sample to accelerate the emitted electrons beyond the spectrometer's minimum measurable energy. In the present experiment it was 1.3eV. The spectrometer was placed normal to the surface to avoid refraction of emitted electron by biasing (Fig. 3-2-2). The refraction will cause the broadening of the lower energy side cut-off and increase the apparent value of work functions. This configuration is also valid for the measurement of the electron distribution at $\Gamma$-point in the Brillouin zone.

In Figure 3-3-1 photoemission spectra of (a) $ZrSe_2$ and (b) Au-foil both taken with $E_A=3.0V$ are shown. Here we define, $E_z$ and $E_v$, low energy side cut off and valence band maximum at $\Gamma$-point of $ZrSe_2$, respectively; $E_g$ and $E_F$ are low energy side cut off and Fermi level of gold, respectively. Work function $\Phi$ and photothreshold $E_p$ of each materials are calculated as follows:

$$\Phi(ZrSe_2) = h\nu - (E_F - E_z) . \qquad (3\text{-}3\text{-}1)$$

$$E_p(ZrSe_2) = h\nu - (E_v - E_z) . \qquad (3\text{-}3\text{-}2)$$

$$\Phi(Au) = E_p(Au) = h\nu - (E_F - E_g) . \qquad (3\text{-}3\text{-}3)$$

Here on the derivation of $E_p$, we have used the equivalence of the photothreshold with the energy difference between the vacuum level and the valence band maximum, which is located near $\Gamma$-point for all of $MX_2$ measured here [7]. We have performed the measurements by applying various $E_A$ between 2.0V and 5.7V for every material, but no observable changes in determining $\Phi$ and $E_p$ have resulted. This suggests that the refraction of electrons is negligible.

The $MX_2$ samples except $2Ha\text{-}TaS_2$ were single crystals larger than 6mm x 6mm grown by vapor transport method with iodine as a transport agent. $2Ha\text{-}TaS_2$ were prepared by heating $1T\text{-}TaS_2$ at 350°C for 24 hours under ultrahigh vacuum (UHV) condition. These samples are mounted on Al disks with conductive resin and cleaved under the vacuum better than 1 x $10^{-6}$ Pa. In order

to confirm the cleanliness and the crystallinity of the samples, they were transferred, with keeping UHV condition, to the other chamber equipped with x-ray photoelectron spectroscopy (Surface Science Instruments ESCA-100 system) and Low Energy Electron Diffraction apparatus (Microscience). Afterwards the sample was transferred to the chamber where the measurement of the work function was performed. The base pressure of the chamber was $1 \times 10^{-8}$ Pa and no effect indicating sample contamination was observed. A gold foil used for the reference was prepared by cleaning with $Ar^+$ ion spattering. The sample temperature was 297K unless otherwise stated.

### 3-3-3 Result

In Table 3-1 experimentally determined work functions and photothreshold values are summarized. The results were reproducible within $\pm 0.1$eV for the measurements on different specimens of the same materials. The work function of gold is consistent with the reported values [8], which confirms the accuracy of the results. We have also investigated the temperature dependence of the work function of $1T\text{-}TaS_2$ to see any effect on the different CDW states. In Fig. 3-3-2 the temperature dependence of the photoemission spectrum of $1T\text{-}TaS_2$ is shown. In this experiment we found no change in the lower energy side cut-off. The clear difference in the valence band is the effect of gap opening at the Fermi level due to CDW transitions [9].

### 3-3-4 Discussion
A. Comparison with the results of other groups

Reports from other groups are compiled in Table 3-2. WFs of $WS_2$ and $WSe_2$, not measured in the present work, are also included for the reference in chapter 7. As seen from the table, our result agrees with other reports for $MoS_2$, $MoSe_2$, $MoTe_2$ within the error of $\pm 0.1$eV. The discrepancy of 0.4eV in

$ZrSe_2$ is probably due to the different doping because nearly the same method of the measurement is applied in the both research.

B. Comparison with theoretical calculations

All non-metallic $MX_2$ were found to be n-type and the work function of $MoS_2$ agrees with the literature [8]. Since the surfaces of layered materials have no dangling bonds nor surface states, it is reasonable to assume that there is no band bending effect at the surface, whereas it exists in conventional semiconductors. Therefore we can regard the photothreshold as an intrinsic property of the materials. The work function is, on the other hand, not suitable for comparison because it varies depending upon the doping. The band structures of $MX_2$ have been calculated by many groups and recent results have shown good agreement with optical and photoemission experiments. While an attempt has been made to estimate the photothresholds for conventional semiconductors like Si and GaAs [10], comparison with experiments is not simple due to the existence of surface recombination. We show, however, such attempts are particularly useful for $MX_2$. In the literature we have found three calculations on $MX_2$ applicable to the present discussion on the photothresholds: semi-empirical method by Bromley, Murray and Yoffe (BMY) [11], *ab initio* tight binding calculation by Bullet (B) [12], and layer method by Woolley and Wexler (WW) [13]. Their results of the photothresholds, derived from their tables and diagrams as the negation of valence band maximum energies, are shown in Table 3-3 and compared with the value from the present experiment (EXP). It is expected that the calculated photothresholds have different offset energies depending on the calculation methods used; therefore, a constant as ascribed below is subtracted from each calculation. In calculation B, a constant 1.8eV is subtracted so as to adjust the energy offset in $ZrSe_2$. Energy offset values of 3.1eV and 5.3eV for WW and BMY were determined from $NbSe_2$ and $MoS_2$, respectively so as to equate the values to those of B. In this way, we have

recalculated the photothresholds for various materials, of which results are tabulated in 'CAL'.

There is good agreement between the calculation and present experiments except for molybdenum compounds. This discrepancy would be partly due to the semi-empirical nature of BMY, while the descending order from $MoS_2$ to $MoTe_2$ have been reproduced correctly.

The difference for $NbSe_2$ might be due to the metallic nature of this compound which is not considered in the band calculations. Lang and Kohn have calculated the effect of electronic double layer caused by the tunneling of free electrons at the surface using a jellium model [2]. Theoretical contribution from free electrons of $NbSe_2$ (one electron / 64.7 $Å^3$) to the work function is read from the graph in [2] to be about +0.4eV, which was at least close to the observed difference (+0.3eV) in the present experiment.

We have observed no change in the work function of $1T$-$TaS_2$ through different CDW states whereas its resistivity changes more than one order of magnitude at the CDW transition around 200K. With Lang and Kohn's theory described above we can speculate that the number of free electrons are so small that its contribution to the work function is negligible even in the low resistivity state of $1T$-$TaS_2$.

The work function of $1T$- and $2Ha$-$TaS_2$ differs as much as 0.4eV while they have identical chemical formula and $1T$ has only 1.3% smaller density than $2Ha$ [14]. We consider the difference in the work function is arising from their structures themselves because a change in the band structure with polytype has been attributed to the different Ta (5d) level splitting in octahedral ($1T$) and trigonal prismatic ($2Ha$) crystal field [15]. Further clarification for this problem is obviously needed.

## 3-4. Possibility of measuring "local work function" by STM

Recent evolution of STM has paved a way for the atomically localized measurement of the surfaces. In this sense, it is foreseeable that the measurement of something like "local WF" might become important in the near future. However, WF is the quantity defined for a whole surface with infinite areas, although it can be different by the index of the faces. In the discussion of thermodynamics, the WF should not be changed by the choice of the path in which the electron are transported from the solid to some place outside the surface (Fig. 3-4-1). For example, path 1 and 2 in the Fig. 3-4-1 gives different values of WF when the WF of metal "A" and "B" are different. Therefore it is convenient to define that the WF is not changed by the lateral difference of location. In this context, the use of the term "local barrier height" instead is accepted for the cases in which the specimen's surface consists of materials with different WFs. It is well established in the field of FEM / FIM that the local difference of the barrier height is compensated by static electric field outside the surface called "patch field" and that the WF is constant as a whole surface [1c].

Now let us consider how to measure the local barrier height by STM. Suppose the tunnel current J can be written with some known and well-defined model function f as:

$$J = B \exp(- f(s, h, h_p)) \qquad (3\text{-}4\text{-}1)$$

where s is the tip-surface distance, B is a factor independent of s, h is the barrier height, $h_p$ is the barrier height characteristic of the probe. If we further suppose that we can measure the function g defined by:

$$g(s) = \frac{\partial \log(J)}{\partial s} = -\frac{\partial f(s, h, h_p)}{\partial s}. \qquad (3\text{-}4\text{-}2)$$

Then the knowledge of $h_p$, g(s) from the experiment, along with the well defined model function f, will enable us to deduce the barrier height h. However, it will be extremely difficult to make a tip with well defined f because we must know the precise atomic arrangement of the tip over some tens of nm to construct the

model. Probably because the difficulty is pronounced, no reports of the experimental results have been published yet.

### 3-5. Conclusion and outlook

Work functions and photothresholds of layered metal chalcogenides ($ZrSe_2$, $HfSe_2$, $NbSe_2$, $1T\text{-}TaS_2$, $2Ha\text{-}TaS_2$, $MoS_2$, $MoSe_2$, $MoTe_2$, $SnS_2$, $SnSe_2$) have been measured by secondary electron threshold method using UPS. The obtained values of work functions and photothresholds will be useful for the wide range of surface and interface study of these materials. From the measurement of temperature dependence, it was found that the charge density waves of $1T\text{-}TaS_2$ have exhibited no observable effect on the WF.

Table 3-1: Work functions and photothresholds (unit: eV).

| material | work function | photothreshold |
|---|---|---|
| $ZrSe_2$ | 5.2 | 6.1 |
| $HfSe_2$ | 4.9 | 6.1 |
| $NbSe_2$ | 5.9 | 5.9 |
| $1T\text{-}TaS_2$ | 5.2 | 5.2 |
| $2Ha\text{-}TaS_2$ | 5.6 | 5.6 |
| $MoS_2$ | 4.8 | 5.6 |
| $MoSe_2$ | 4.4 | 5.5 |
| $MoTe_2$ | 4.1 | 5.0 |
| $SnS_2$ | 5.2 | 7.4 |
| $SnSe_2$ | 5.3 | 6.4 |
| Au | 5.3 | 5.3 |

Table 3-3 : Comparison with calculated photothresholds (unit: eV).

| $MX_2$ | CALCULATIONS | | | | EXP | EXP-CAL |
|---|---|---|---|---|---|---|
| | WW | B | BMY | CAL | | |
| $ZrSe_2$ | | 7.9 | | 6.1 | 6.1 | 0.0 |
| $HfSe_2$ | | 7.9 | | 6.1 | 6.1 | 0.0 |
| $NbSe_2$ | 8.7 | 7.4 | | 5.6 | 5.9 | +0.3 |
| $1T\text{-}TaS_2$ | 8.1 | | | 5.0 | 5.2 | +0.2 |
| $2Ha\text{-}TaS_2$ | 8.7 | | | 5.6 | 5.6 | 0.0 |
| $MoS_2$ | | 7.8 | 11.3 | 6.0 | 5.6 | -0.4 |
| $MoSe_2$ | | | 11.3 | 6.0 | 5.5 | -0.5 |
| $MoTe_2$ | | | 9.8 | 4.5 | 5.0 | +0.5 |

Table 3-2: Comparison of present results with other studies (WF only, in eV). Letters in [] show the reference number. # is the present experiment. Methods of the measurement are (p) is photoelectron yield, (t) is secondary electron threshold, (k) is Kelvin method, and (r) is the retardation voltage method.

| material(dopant) | | WF | Ref. (method) |
|---|---|---|---|
| $ZrSe_2$ | (n) | 5.2 | # |
| $ZrSe_2$ | (n) | 4.8 | [8a](t) |
| $HfSe_2$ | (n) | 4.9 | # |
| $NbSe_2$ | | 5.9 | # |
| $1T-TaS_2$ | | 5.2 | # |
| $2Ha-TaS_2$ | | 5.6 | # |
| $MoS_2$ | (n) | 4.8 | # |
| $MoS_2$ | - | 4.8 | [8b](r) |
| $MoS_2$ | (n) | 4.8 | [8c](p) |
| $MoS_2$ | (n) | 4.9 | [8d](p) |
| $MoS_2$ | (p) | 5.2 | [8e](p) |
| $MoSe_2$ | (n) | 4.4 | # |
| $MoSe_2$ | (n) | 4.6 | [8e](p) |
| $MoTe_2$ | (n) | 4.1 | # |
| $MoTe_2$ | (i) | 4.3 | [8f](p) |
| $WS_2$ | (n: ~$10^{17}$) | 4.4-4.7 | [8g], [8h](p) |
| $WSe_2$ | - | 4.9 | [8i](r) |
| $WSe_2$ | (n: ~$10^{17}$) | 4.1 | [8j](t) |
| $WSe_2$ | (p: ~$10^{17}$) | 5.6-5.0 | [8k](t) |
| $SnS_2$ | (n) | 5.2 | # |
| $SnS_2$ | (n) | 4.4 | [8h](p) |
| $SnS_2$ | - | (6.3p) | [8l](p) |
| $SnSe_2$ | (n) | 5.3 | # |
| $SnSe_2$ | - | (5.35p) | [8l](p) |
| Au | | 5.3 | # |
| Au | | 5.3 | [8k] |
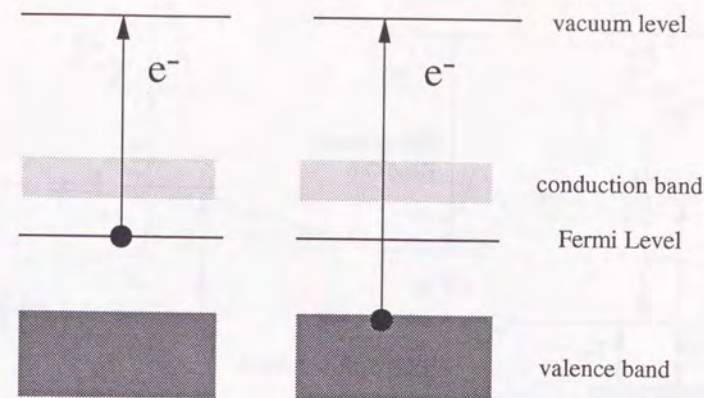


Fig. 3-1-1: Definition of the work function and photothreshold in the case of a semiconductor. In metals and semimetals, the work function and the photothreshold have the same value.
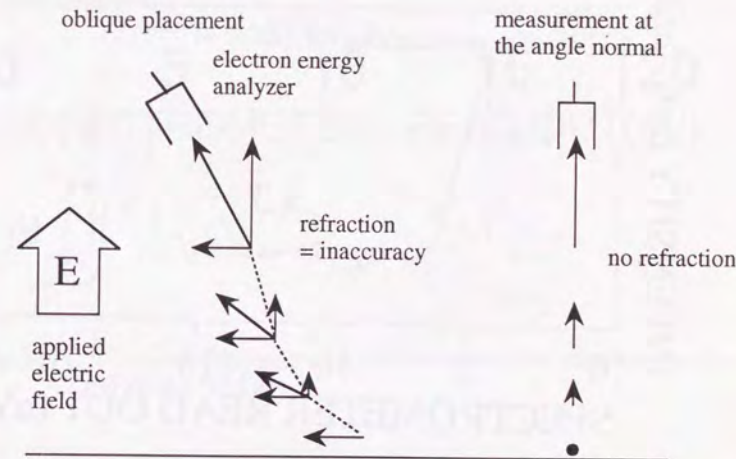


Fig. 3-2-2: The need of angle resolution in the work function measurement by secondary electron threshold method.

sample  electron energy analyzer  sample  electron energy analyzer

$h\nu$

$E_1$

Spectrometer Read Out

$E_{vac}$  $E_{vac}$  $E_2$

$e\Phi$

$eV_{sp}$  $eV_{sp}$

$E_F$

$e\Theta$  $E_v$

electrical contact

valence band

$E_1 = h\nu - eV_{sp}$

$E_2 = e\Phi - eV_{sp}$

$e\Phi = E_1 - E_2 - h\nu$

$e\Theta = e\Phi + E_v$

UPS of a semiconductor (ZrSe$_2$)

$E_2$

x 3

$E_v$

$E_1$

INTENSITY (arb. unit)

SPECTROMETER READ OUT (eV)
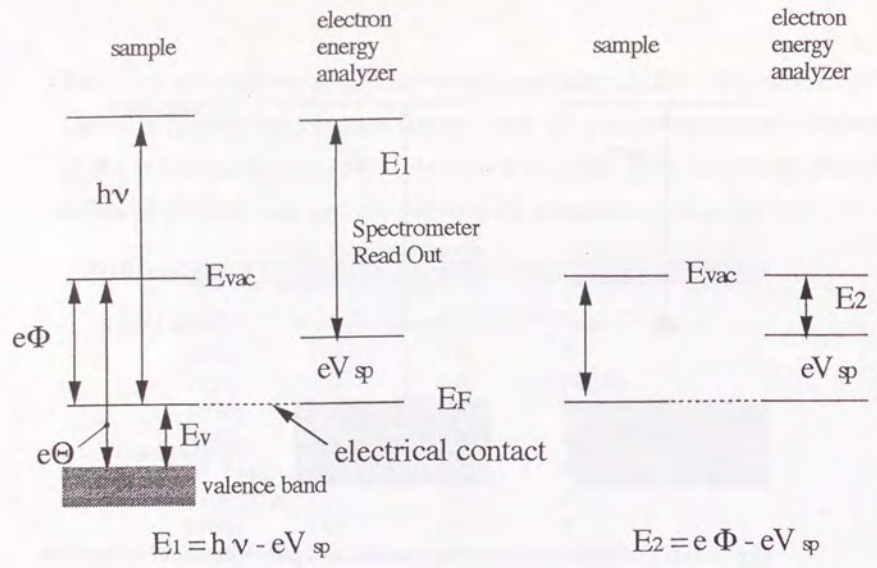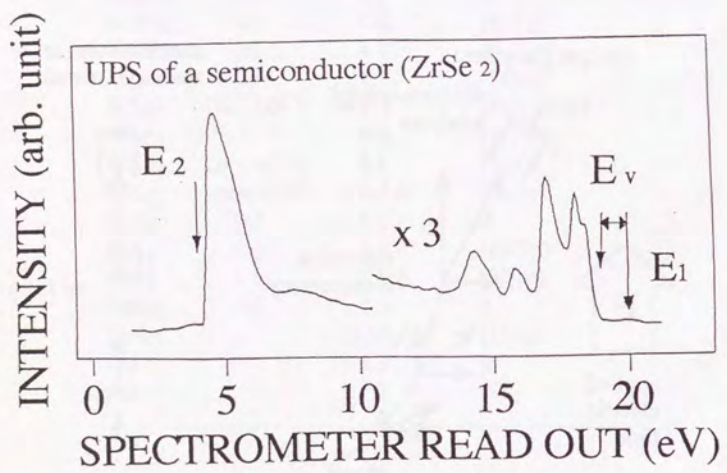
Fig. 3-2-1: Measurement of the work function ($e\Phi$) and photothreshold ($e\Theta$) by secondary electron threshold method.
$E_F$: Fermi level; $E_{vac}$: vacuum level;
$eV_{sp}$: offset of spectrometer; $h\nu$: photon energy.



(a)

$E_z$  x 3  $E_v$

(b)

$E_g$  x 3  $E_F$

INTENSITY (arb.unit)

SPECTROMETER READ OUT(eV)
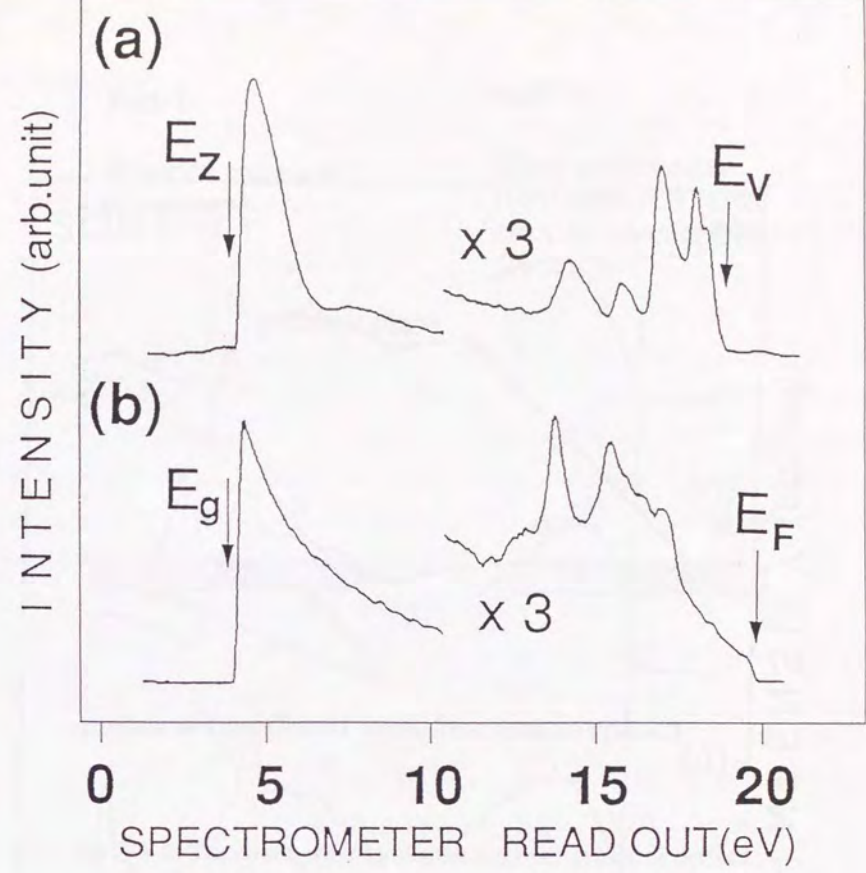
Fig. 3-3-1: Ultraviolet photoemission spectra taken at the normal exit angle.
(a) ZrSe$_2$ (b) Au.
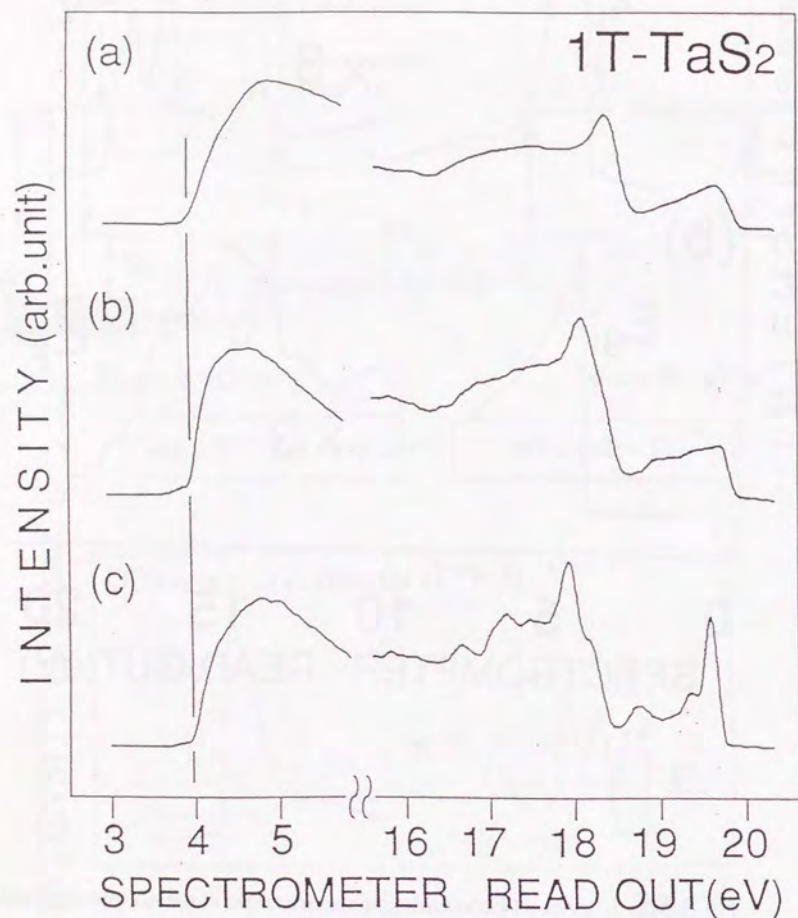
Fig. 3-3-2: Temperature dependence of the photoemission spectra ( Γ-point) of 1T-TaS 2. (a) 380K (incommensurate CDW), (b) 295K (nearly commensurate CDW), (c) 150K (commensurate CDW). Note that the low energy side cut-off does not change.

Path 1

Electron emission from metal "A"

Path 2

Electron emission from metal "B" after electron transfer from "A" to "B"



a distant place

A          B          A          B

metals with different work functions in contact
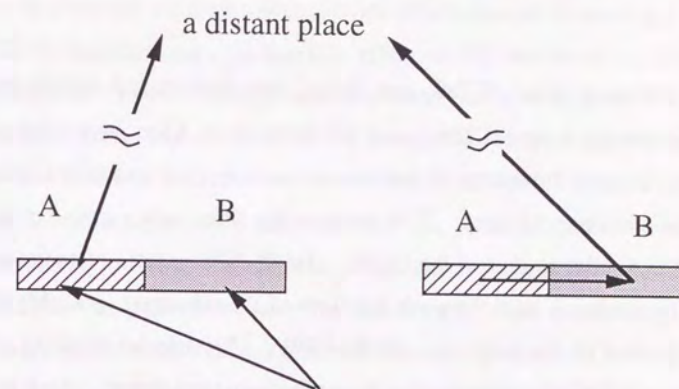
Fig. 3-4-1: The reason why "local work function" cannot be defined.

# Chapter 4. Polytypes and charge density waves of ultrathin TaS$_2$ and TaSe$_2$ films grown by van der Waals epitaxy

Ultrathin films of TaS$_2$ and TaSe$_2$, two-dimensional metals known for charge density waves (CDWs) and polytypes, have been grown epitaxially on various layered substrates by molecular beam epitaxy and characterized with surface science techniques. STM image of the films shows irregular modulation which is similar to that of the CDW. Ta(4f) XPS spectra of monolayer films have a correlation with the work functions of the substrates, probably due to the modification of the polytypes and the CDWs. Electric conductivity of the film grown at 350°C shows anomalous dependence on temperature, which is probably related to the occurrence of CDW in a disordered crystal.

## 4-1. Introduction

Charge density waves (CDWs) have been of particular interest in solid state physics[1]. The CDW states are characterized with periodic lattice distortions and charge density modulations, which are induced by the Fermi-surface-driven structural instabilities. Although CDW is a phase transition of a two dimensional electronic structure, the effects caused by making a thin film of a CDW material, e.g., (i) the size effect or (ii) the interface effect are not understood *a priori*. In spite of a long history of investigation, few reports are found on these aspects of CDW. The studies for (i) includes 'free-standing monolayer films' fabricated by the exfoliation of bulk TaSe$_2$. The report says that the monolayer films did not show the periodic lattice distortion when observed by transmission electron diffraction at low temperature [2]. For (ii), the effect of charge transfer, in particular, seems promising for a new phenomenon. Although the effect of charge transfer on CDW is studied by intercalation [3] or doping [1], there are fundamental limitations in those approach. It is accepted that the chemical species which can be intercalated to CDW materials are only electron donating ones [3] and the effect of decreasing the electron density in CDW has not been studied experimentally. By the doping method, dopants act as defects in the crystal as well as the agent to change the electron density. I therefore attempted the epitaxial growth of ultrathin films of a CDW material on various substrates and the measurement of physical properties including CDW.

Here VDWE was applied to fabricate films of TaS$_2$ and TaSe$_2$ with 1ML ~ 16ML thickness on various substrates including HOPG, MX$_2$, and Se-terminated GaAs(111). These CDW materials were chosen because various data have been accumulated on their conspicuous CDW transitions. They are also known to have many different crystal structures called polytypes. Although polytypes change CDWs drastically [1], the mechanism of the formation of various polytypes is not known. Our results will be analyzed by taking into account also

this aspect of the material. The grown films were characterized with reflection high energy electron diffraction (RHEED), x-ray photoelectron spectroscopy (XPS), and scanning tunneling microscopy (STM). Temperature dependence of electric conductivity was also measured from 0.45K to 300K.

## 4-2. Experiment

The substrate materials are shown in Table 4-1 with their lattice constants [4], work functions (WFs) and photothresholds [5]. Single crystals of transition metal dichalcogenides ($MX_2$) substrates were grown by halogen vapor transport with iodine as the transport agent. Graphite was c-axis aligned highly oriented pyrolytic graphite (HOPG). $NbSe_2$ and HOPG were metallic and semimetallic, respectively, while other $MX_2$ substrates were all n-type semiconductors as seen from XPS valence band spectra.

The substrates with (0001) surfaces were prepared by cleaving under ultrahigh vacuum and transferred to a turbo-molecular-pumped growth chamber with a base pressure of $8 \times 10^{-8}$ Pa. Epitaxial growth was carried out in the excessive sulfur condition. Sulfur beam was generated by a sublimation source while tantalum was evaporated from a Joule-heated wire with a purity of 99.95%. The partial pressure of sulfur was between $1 \times 10^{-3}$ and $1 \times 10^{-4}$ Pa during the growth. The growth rate of $TaS_2$ and $TaS_2$ was monitored by a quartz oscillator and was about 0.1 nm / min. This value was consistent with the time in which RHEED pattern changed from that of the substrate to that of the grown film. The substrate temperature ($T_{sub}$) attempted for the growth were between 250°C and 650°C. The XPS system was Surface Science Laboratory's ESCA-100 of which energy resolution was calibrated from Au (4f) core level spectra as 0.7eV in FWHM. STM measurement was performed with Digital Equipment's Nanoscope II with a W-tip in constant current mode with 2 ~ 4 nA tunneling current. Electric conductivity of the films was measured by four-probe method using gold wire ($\phi$ 50µm) electrodes bonded with silver paste to

the surface of the films. The temperature of the specimen was controlled in the sample space of Magnetic Property Measurement system (MPMS) (Quantum Design) from 300K to 1.87K. Below the liquid He temperature (4.2K), a $^3$He cryostat was utilized (chapter 2).

## 4-3. Epitaxial growth condition and polytypes of the films

The properties of the films were dependent on the thickness, growth temperature ($T_{sub}$), and substrate materials. First we focus on the films thicker than 5 monolayers (ML) of which surface properties appeared to be independent of the substrates. Judging from RHEED patterns, $T_{sub}$ was the only important factor determining the crystallinity of the films. RHEED streak patterns corresponding to a hexagonal lattice with a lattice constant of $3.4 \pm 0.1$ Å were observed when the films were grown on $MX_2$ substrates with $T_{sub}$ between 330°C and 600°C. This lattice constant agrees with the value of the bulk within error. The direction of the axes of the films were aligned with those of the substrates. Since HOPG substrate consists of polycrystals aligned only in c-axis direction perpendicular to the surface, RHEED pattern from the films on HOPG was columnar one corresponding to a rotated hexagonal lattice with the same lattice constant. Although RHEED only showed that the films grown at lower $T_{sub}$ give slightly broader streak patterns than those at higher $T_{sub}$, XPS revealed that two different kinds of films were formed depending on the $T_{sub}$. Two different peak shapes of Ta($4f_{7/2}$) core level XPS were identified as shown in Fig. 4-3-1. A round shape (Fig.(a)) and a skew triangle shape (Fig.(b)) were observed from the films grown under the conditions of $T_{sub}$=330~370°C and $T_{sub}$=420~600°C, respectively. These films are referred as L-films (grown at low temperatures) and H-films (grown at high temperatures) in the following. When the L-films were heated above 420°C, they were converted to H-films irreversibly. Binding energies of S($2p_{3/2}$) core levels of the films are also shown in Fig. 4-3-1 for the comparison with those of the bulk.

TaS$_2$ is known for its abundant polytypes, which can be regarded as the combination of octahedral coordination (OC) and trigonal prismatic coordination (TP) in the stacking of layers. Since it is expected that the difference in the coordination may be reflected in the Ta core level in XPS, Ta (4f$_{7/2}$) spectra of bulk 1T-TaS$_2$ (all OC stacking) and 2Ha-TaS$_2$ (all TP stacking) have been measured as shown in Fig. 4-3-2. The experiment was performed at various temperatures to illustrate the effect of CDWs on the spectra, yet the measurement above 360K was not feasible because 1T undergoes a polytype transformation above this temperature. While the spectra depend on the temperature because of the CDW [6], the difference in the peak position at 360K, by about 0.4eV, is noticeable. At this temperature CDWs of 1T- and 2Ha-polytypes are incommensurate and absent, respectively, and therefore their effects on Ta core level spectra are probably smallest. Since CDWs of OC and TP layers occur almost independently of each other [7], electronic structures of those layers are basically intrinsic to each layers. Thus XPS Ta (4f$_{7/2}$) spectra of the grown films are compared with those of bulk 1T and 2Ha for fingerprinting in the followings.

After prolonged observation by STM, the surface of the films exhibited a characteristic morphology as shown in Fig. 4-3-3. It is reported that the triangular shapes were observed from other layered materials [8]. They were identified as etch patterns due to STM rastering similar to those observed after chemical etching of crystal surfaces. In the chemical etching, the orientation of the etch pits reflects that of the crystals. Although the atomic arrangement of the top surface of the films showed hexagonal symmetry when observed with RHEED or STM, one molecular layer of TaS$_2$ have three fold symmetry whichever coordination the layer has. It is therefore expected that the triangular etch patterns indicate the crystallographic orientation of each layer. The scanned area shown in Fig. 4-3-3 contains three successive layers which are identified with the intensity of the image. The etch patterns are pointed by circles marked

with the layer number counted from the top surface. Since the triangular etch patterns of all layers have the same direction, these layers presumably have the same orientation.

By comparing XPS of our films (Fig. 4-3-1) with those of bulk samples (Fig. 4-3-2), it is found that both Ta and S core levels of H-films are identical to those of bulk 2Ha-TaS$_2$. On the other hand, Ta(4f$_{7/2}$) core level of a L-film resembles that of 1T-TaS$_2$ in incommensurate CDW state, while the binding energy of S(2p$_{3/2}$) was intermediate value of bulk 1T and 2Ha. The latter observation indicates that a L-film consists mainly of OC with small amount of TP, which lowers the S(2p$_{3/2}$) core level. It is reported that bulk 1T-TaS$_2$ transforms to 2Ha irreversibly when heated above 450K [9] while it was observed that our L-films converted to H-films irreversibly when heated. This similarity suggests that main portion of our L-films is 1T-TaS$_2$. Etch patterns found during STM measurements (Fig. 4-3-3) also support this interpretation. Since the triangular etch pattern had the same direction in three successive layers, these layers had the same crystallographic orientation. The commonly formed polytypes of OC and TP are 1T and 2Ha, respectively, and in 1T all layers have the same direction while in 2Ha the layers have alternating direction. Our observation in Fig. 4-3-3 is in accordance with the identification that a L-film is mainly 1T.

It should be noted that the growth condition is different from the bulk crystal growth. Bulk TaS$_2$ is usually grown with halogen vapor transport in which TaS$_2$ powder and halogen gas are sealed in a quartz tube, and temperature gradient around 900°C is maintained for several weeks [10]. OC-TaS$_2$ is not thermodynamically stable below about 500°C [11] and it transforms to TP when the vessel is cooled slowly to room temperature. Thus single crystals of OC are only obtained by quenching from the growth temperature. It was found, nevertheless, OC-like portion is formed in L-films at $T_{sub}=350\pm20°C$. This is an indication of non-equilibrium nature of MBE.

Similar result was obtained for $TaSe_2$. The threshold temperature for the OC-TP transition was $400\pm20$ °C.

## 4-4. Evidence for charge density waves in the films

### 4-4-1 STM

STM images were observed from L-films grown on $MoTe_2$ and $MoSe_2$. Figure 4-4-1 shows an atomic image of a 5 ML film grown on $MoTe_2$, in which an irregular modulation in the contrast is clearly observed along with hexagonal lattice of $TaS_2$. For both of $MoTe_2$ and $MoSe_2$ substrates the scale of the modulation in $TaS_2$ films was always 10~20Å despite the difference in their lattice constants. On other substrates, atomic images were not observed because of severe etching by STM tips.

STM of $1T\text{-}TaS_2$ shows $\sqrt{13} \times \sqrt{13}$ superstructure due to CDW at room temperature, while TP-layers in both of $2Ha\text{-}TaS_2$ [12] and $4Hb\text{-}TaS_2$ [13] do not show any superstructure at the room temperature. The mottled STM images with atomic resolution (Fig. 4-4-1) suggest CDW of $1T\text{-}TaS_2$ is disturbed and probably 'frozen' by the defects due to the mixed TP- sites.

### 4-4-2 Temperature dependence of XPS Ta(4f7/2) core level

Since CDW is the temperature dependent phase transition, Ta $(4f_{7/2})$ core emission from the L-films were observed at different temperatures (Fig. 4-4-2). Gradual broadening was identified as the temperature was decreased. A subtraction spectrum (Fig.(c)) emphasizes this difference. In contrast to the L-films, XPS of the H-films showed no temperature dependence.

Observed broadening of $Ta(4f_{7/2})$ peak shape of L-film at low temperature indicates a certain portion of the film changes its electronic structure with the temperature change. It is probably due to the occurrence of CDW transition in the well defined OC-areas.

### 4-4-3 Anomaly in the dependence of electric resistivity on temperature

Two kinds of evidence mentioned above was obtained for $TaS_2$ films. However, the resistivity measured in the present research was not of $TaS_2$ films, but of $TaSe_2$ films. Since other properties of the films were nearly the same for both of $TaS_2$ and $TaSe_2$, it is expected that the electric resistivity also shows similar behavior for $TaS_2$ and $TaSe_2$.

The temperature dependence of the electric resistivity of L-film and a H-film of $TaSe_2$, is shown in Fig. 4-4-3. The H-film has nearly constant resistivity from 0.45K to 300K, which is understood as a behavior of a metal with disorder. On the other hand, the resistivity of the L-film increases more than 30 times when cooled from 300K to 1.87K and it saturates below 10K. This increase with saturation is not explained by thermal-activation type conductivity of a semiconductor or a metal with an island structure. For comparison, the resistivity of various polytypes of $TaSe_2$ and $TaSe_3$ are shown in Fig. 4-4-4 [1,14]. The result of our L-film cannot be reproduced by the combination of these bulk behavior. The increases of resistivity with hysteresis associated with CDW transition in 1T(~473K) and OC-layer in 4Hb-type(~315K) are accepted as the indication of partial extinction of Fermi-surface due to CDW transition. The result for the L-film can be understood by a model in which CDW transition takes place continuously at different temperatures site by site. This model of gradual occurrence of CDW is consistent with the above observation with STM and XPS.

## 4-5. Monolayer films

### 4-5-1 Results

Strong substrate dependence was found when films with nearly 1ML thickness were fabricated at 330~370°C (condition for L-films). The growth was stopped when the RHEED streak patterns of the films became clear and those of the substrates just decayed. Figure 4-5-1 shows the Ta(4f7/2) core level

spectra of these films with lattice constants and WFs of the substrates. It is noticed that the peak shapes change correspondingly with the WFs of the substrates. Those differences were much weakened when the films were thicker than 2ML. The binding energies of the core levels of the substrates, which were 'seen through' the films because of their small thickness, are tabulated in Table 4-2 with those of sulfur of $TaS_2$ films. The binding energies are shifted by the same value for both of the metal and chalcogen elements in the substrate materials. This indicates the shifts are due to the band bending of the substrates and that no reaction took place between the film and the substrates. As for the $NbSe_2$ and HOPG substrates the binding energy of the substrate elements did not change. For higher $T_{sub}$ (condition for H-films) the result was not so reproducible as L-condition, probably because of the partial decomposition of the substrates.

## 4-5-2 Discussion

Since in the photoemission the photoelectrons corresponding to the Fermi level are always detected at the same kinetic energy irrelevant to the WF of the substrates, the difference in the peak position of $Ta(4f_{7/2})$ core levels must be due to the different electronic structure of the films. Although an exception to above rule is discussed recently regarding the shift of binding energy of the metals due to a photovoltaic effect at Schottky interfaces [15] , our observation cannot be explained by that mechanism. That effect arises from the photovoltaic electromotive force caused by the photons of the source x-ray in the photoemission experiments. In the case of the n-type semiconductor Schottky junction, it will shift the core levels of the films to higher binding energy when the substrate has lower WF, which is opposite to our observation.

The observed peak binding energies of $Ta(4f_{7/2})$ core levels are shifted in the descending order of the WF difference with the exception of HOPG and $NbSe_2$ substrate. These two were the only non-semiconductive substrates used in

the present experiments. In order to elucidate the nature of this observation, the films grown on those substrates are examined first. The possibility of interfacial reaction is not likely because the core level spectra from the underlying substrates were identical with those from the clean surface of the materials. As shown in Fig. 4-5-2, the XPS Ta ($4f_{7/2}$) and S ($2p_{3/2}$) from the 1ML films on $NbSe_2$ and HOPG grown at the L-film condition were almost the same with those from thick L- and H-films, respectively. Namely, on HOPG, the polytypes of surface layers of the films grown at low $T_{sub}$ changed from OC to TP when the thickness is reduced, while thick L-film structure is maintained on $NbSe_2$ even at 1ML thickness. This indicates the polytype near the interface is controlled by the substrates.

In order to account for the present finding, it should be noted that the WFs are different between 1T and 2Ha-$TaS_2$. Although there is no measurement of the WFs of $TaS_2$ with 1ML thickness, it is acceptable that the WFs of OC and TP are well represented by those of 1T and 2Ha because the electronic structures are determined almost layer-by-layer as discussed above. A model related to the electrostatic energy of the metal-metal or metal-semimetal van der Waals interfaces is constructed as follows (Fig. 4-5-3). When two metals or semimetals with inert van der Waals surfaces are connected, a large term of the interface energy will be due to the electrostatic one arising from the electric dipole layer to compensate the WF difference. In the classical approximation, the energy per unit cell E is estimated as that of a capacitor as following:

$$E = (1/2) C \Delta\Phi^2 ; \quad C = \varepsilon \varepsilon_0 S / d, \quad (4-5-1)$$

where $\Delta\Phi$ is the WF difference, S is the interface area per Ta atom, d is the distance of the interfaces, $\varepsilon_0$ is the dielectric constant of vacuum, and $\varepsilon$ is the relative dielectric constant of the interface.

Applying an underestimation that $\varepsilon=1$ and putting S=10 $Å^2$, d= 3Å, and $\Delta\Phi=1$ V, the value E=0.018 eV / Ta atom or 0.42 kcal / mol is obtained. This energy stabilizes the interface with lager WF difference, which agrees with our

results. The number of charges involved in the calculation above is 0.018 $e^-$ / Ta atom, which will be small enough to validate the assumption that the change in the electronic structure of the substrate is negligible. This assumption is consistent with the fact that no band bending was observed in the substrates. The model also explains the observation that the films thicker than 2ML did not show the difference in XPS: the electrostatic effect would be shielded in the thicker films and consequently the polytype at the surface observed with XPS are controlled only by the temperature condition.

This model of electrostatic energy can be used to explain the structure of some polytypes as following, which gives the model more credibility. There are polytypes called 4Hb- and 6R- $TaS_2$ made up of alternating OC- and TP- layers and stable for the temperature range between 1T (all OC) and 2Ha (all TP) polytypes [10]. Since the WF of 1T and 2Ha are different as shown in Table 4-1, it follows that the formation mechanism of the alternating layers in these polytypes is also electrostatic stabilization at the interfaces. This hypothesis is also supported by a band calculation of 4Hb-$TaS_2$ [16] in which a charge transfer by 0.08 ~ 0.11 $e^-$ / Ta atom from OC- to TP- layers were observed. The value is even larger than our simple model and justifies our assumption of the charge transfer between conductive layers across van der Waals interfaces.

The spectrum from a film on a $MoTe_2$ substrate resembles considerably with that on HOPG substrate, which suggests the effect similar to above is taking place in this case. Although the formation energy of metal-semiconductor interface has not drawn attention in the literature because it is small in the ordinary combination (section 4-5-3), it is considerably large at the $TaS_2$-$MoTe_2$ interface (Fig.4-5-3(c)). $MoTe_2$ substrate in our experiment was n-type semiconductor with a 0.9eV band gap. Because of the WF of $TaS_2$ (5.2eV and 5.6eV for 1T and 2Ha, respectively) is larger than the photothreshold of $MoTe_2$ (5.0eV), $MoTe_2$ near the interface becomes inverted. Once the inversion occurs at the semiconductor interface, the valence electrons will be transferred to the

metal overlayer. Since the density of states of valence electrons are of the same orders of magnitude with that of metals and semimetals, the number of the carriers transferred are comparable to the case of the metals and semimetals. Consequently, $MoTe_2$ substrate will behave like a metal or a semimetal with about 5.0eV (= photothreshold) WF and the interface formation energy will be comparable to that of $TaS_2$-HOPG interface. This discussion probably explains the similarity of XPS between $TaS_2$ on $MoTe_2$ and $TaS_2$ on HOPG. For other semiconductor substrates, the above model will not work because WFs of $TaS_2$ are larger (in the cases of $MoS_2$ and $HfSe_2$) than or nearly the same (in the case of $MoSe_2$) as the photothresholds of substrates. This is consistent to our observation.

For the semiconductor substrates except for $MoTe_2$, we noticed the $Ta(4f_{7/2})$ core levels consist of two peaks near 23.1eV and 23.7eV and that the ratio changes according to the WF or the photothresholds of the substrates. The peak energies are similar to those of 1T-$TaS_2$ in commensurate CDW (Fig. 4-3-2). The possibility of the mixture of different polytypes in 1ML films is excluded because it is impossible to reproduce the peak shapes from the combination of those of TP and OC without CDW. It is therefore considered that CDW is probably involved in these cases.

The precise mechanism for this observation is not clear yet, but it can be said the difference of electronic structure, such observed in intercalation [3] or doping [17], is not likely the case here. Indeed electrons are transferred at metal semiconductor interface, but the number is several orders of magnitudes smaller than the case of the intercalation or doping (section 4-5-3). The present result is open to theoretical investigation.

*4-5-3 Estimation of electrostatic energy of metal-semiconductor interfaces*

In this appendix, the electrostatic energy of uniform dipole layers at metal-semiconductor interfaces is estimated. When the WFs and photothresholds

of n-type semiconductors are respectively smaller and larger than the WF of the metal, the Schottky barriers are formed (the cases of $MoS_2$, $MoSe_2$ and $HfSe_2$ substrates). The electrostatic energy E per unit cell is calculated by using depletion approximation [18] as:

$$E=(1/3) \, e^{1/2} \, \rho^{1/2}(\varepsilon\varepsilon_0)^{1/2} \, \Delta\Phi^{3/2} \, S \qquad (4\text{-}5\text{-}2)$$

where $\Delta\Phi$ and S are the same as above, e is the charge of an electron, $\rho$ is the carrier density of the n-type semiconductor, $\varepsilon_0$ is the dielectric constant of vacuum, and $\varepsilon$ is the relative dielectric constant of the semiconductor (Fig.4-5-3(d)). Putting $\rho=10^{17} \text{cm}^{-3}$ [19], $\varepsilon=10$, $\Delta\Phi=1$ V, $S=10\text{Å}^2$, $E=3 \times 10^{-4}$ eV is obtained. This is two orders of magnitudes smaller than in the cases of metallic and semimetallic substrates. It is therefore not likely that the polytype changes in this case. The number of charges (n) per unit cell transferred from the semiconductor to the metal is given as

$$n= (2\varepsilon\varepsilon_0\rho V)^{1/2} e^{-1/2} S. \qquad (4\text{-}5\text{-}3)$$

Assuming the values used in the above calculation for E, $n=1.0 \times 10^{-3}$ / unit cell is obtained. It is too small compared to the reported charge transfer by doping or intercalation which changed CDW. $TaS_2$-$MoTe_2$ interface is different from above as discussed in section 4-5-2.

## 4-6. Conclusion and outlook

$TaS_2$ and $TaSe_2$ layered metals with CDW, were grown on various layered substrates by van der Waals epitaxy and characterized with surface science techniques. Two different phases corresponding to the polytypes of $TaS_2$ and $TaSe_2$ were identified depending upon the growth condition. Irregular intensity modulation was observed in STM, which might be due to CDW pinned by defects. The dependence of resistivity of the films on temperature suggests the CDW transition which probably occurs continuously site-by-site at different temperatures. XPS $Ta(4f_{7/2})$ spectra of monolayer films have a correlation with

the WF of the substrates, due to the modification of polytype and CDW. The present result will provide a new insight into the study of interfaces and CDW.

Table 4-1: Lattice constants, work functions and photothresholds of the
substrates and TaS$_2$

| substrate | lattice constants(Å) | work function(eV) | photothreshold(eV) |
|-----------|---------------------|-------------------|--------------------|
| MoTe$_2$ | 3.52 | 4.1 | 5.0 |
| MoSe$_2$ | 3.29 | 4.4 | 5.5 |
| MoS$_2$ | 3.16 | 4.8 | 5.6 |
| HfSe$_2$ | 3.75 | 4.9 | 6.1 |
| NbSe$_2$ | 3.45 | 5.9 | 5.9 |
| HOPG | 2.46 | 4.5 | 4.5 |
| 1T-TaS$_2$ | 3.36 | 5.2 | 5.2 |
| 2Ha-TaS$_2$ | 3.31 | 5.6 | 5.6 |

Table 4-2: Band bending of the substrate MX$_2$ after monolayer films were
grown at $T_{sub}$=350°C. Shifts of the binding energy of the core levels of
constituent elements (M and X) are tabulated with the S($2p_{3/2}$) core level
of monolayer TaS$_2$ in the unit of eV. The sign is defined so that a shift to
the higher binding energy gives plus. In the case of MoS$_2$, it was unable
to separate S($2p_{3/2}$) core level from the film and the substrate.

| substrate | M | X | S($2p_{3/2}$) |
|-----------|------|------|---------------|
| MoTe$_2$ | -0.3 | -0.3 | 161.4 |
| MoSe$_2$ | -0.4 | -0.4 | 161.4 |
| MoS$_2$ | -0.6 | - | - |
| ZrSe$_2$ | 0.0 | 0.0 | 161.1 |
| HOPG | no shift(C(1s)) | | 160.9 |
| NbSe$_2$ | 0.0 | 0.0 | 161.2 |
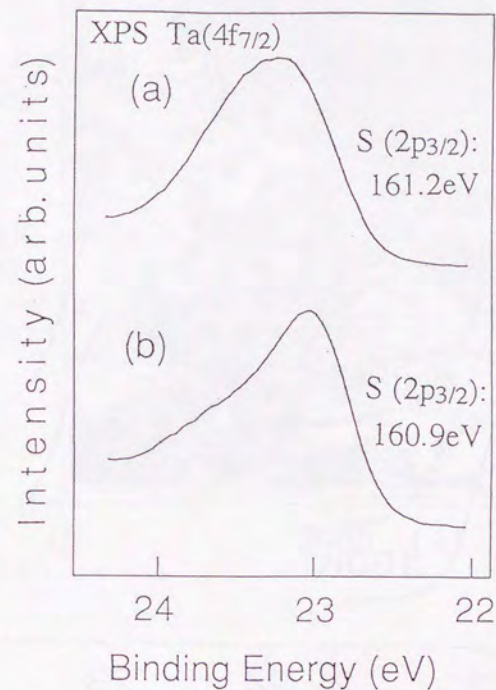


Fig. 4-3-1: XPS Ta($4f_{7/2}$) core levels of the films grown at (a)
330~370°C (L-films) and (b) 420~650°C (H-films).

Octahedral (OC)

Trigonal Prismatic (TP)

Intensity (arb. units)

360K

360K

295K

160K

160K

Binding Energy (eV)

24    23    22    24    23    22
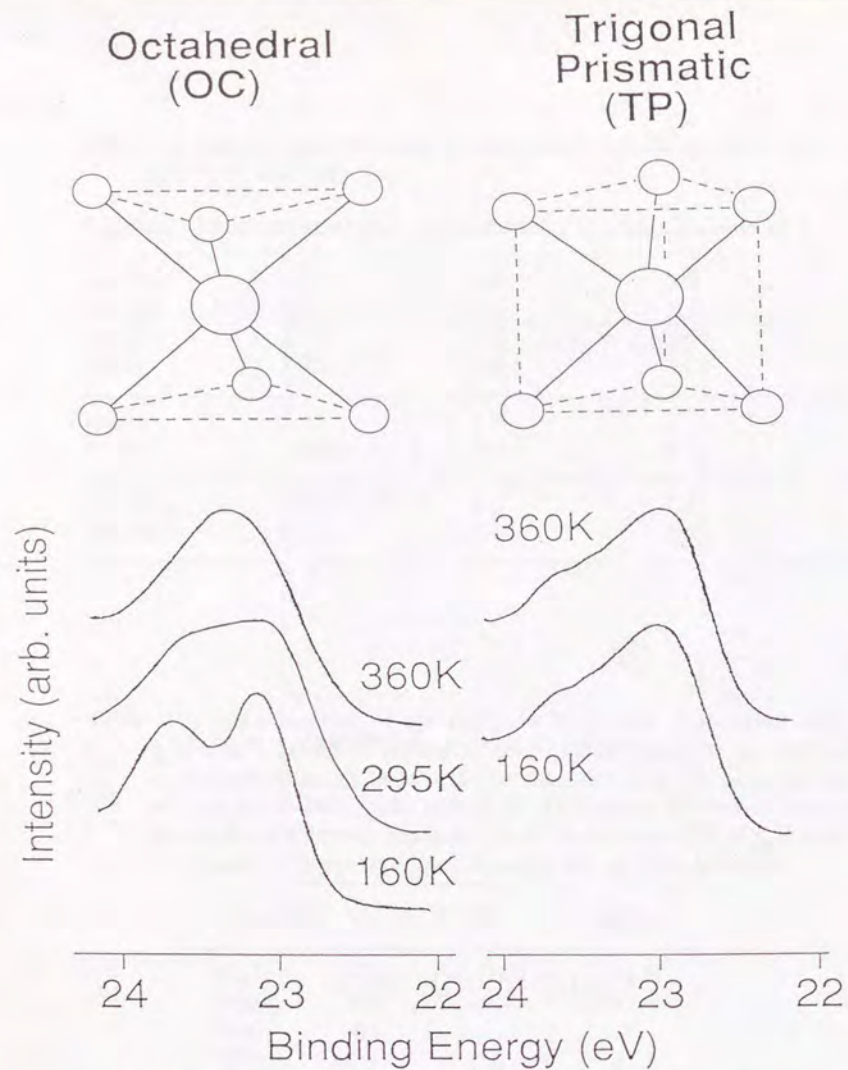
Fig. 4-3-2: XPS Ta($4f_{7/2}$) core levels of bulk 1T-TaS$_2$ (OC) and 2Ha-TaS$_2$ (TP) measured at different temperatures. CDWs of 1T-TaS$_2$ at 360K, 295K and 160K are 'Incommensurate', 'Nearly Commensurate' and 'Commensurate', respectively. While 2Ha-TaS$_2$ is in 'Normal' state at both of 360K and 160K, it is reported that XPS Ta($4f_{7/2}$) does not change even at 'Commensrate'-CDW state below 90K [6].
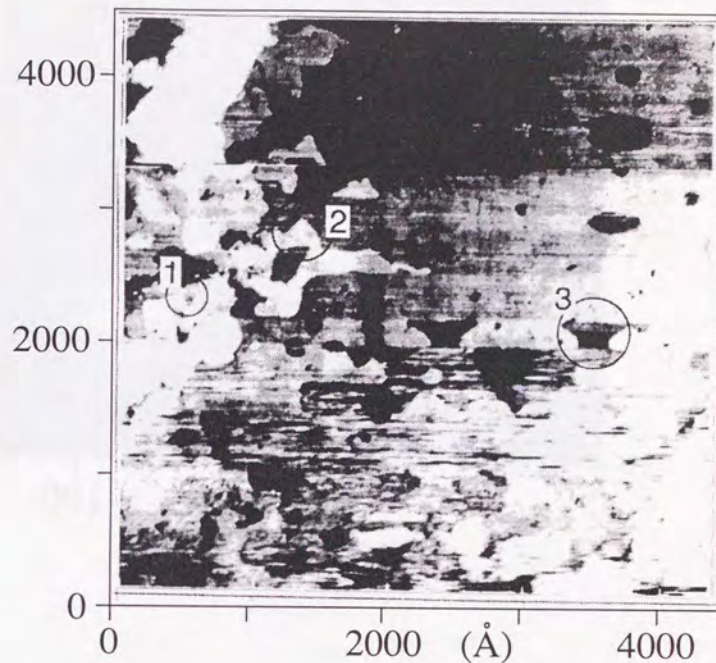


Fig.4-3-3: Etching pattern of a L-film of TaS$_2$ observed with STM.
The numbers with circles indicate the layer number counted from the top surface.

100

50

0

0          50          (Å)    100
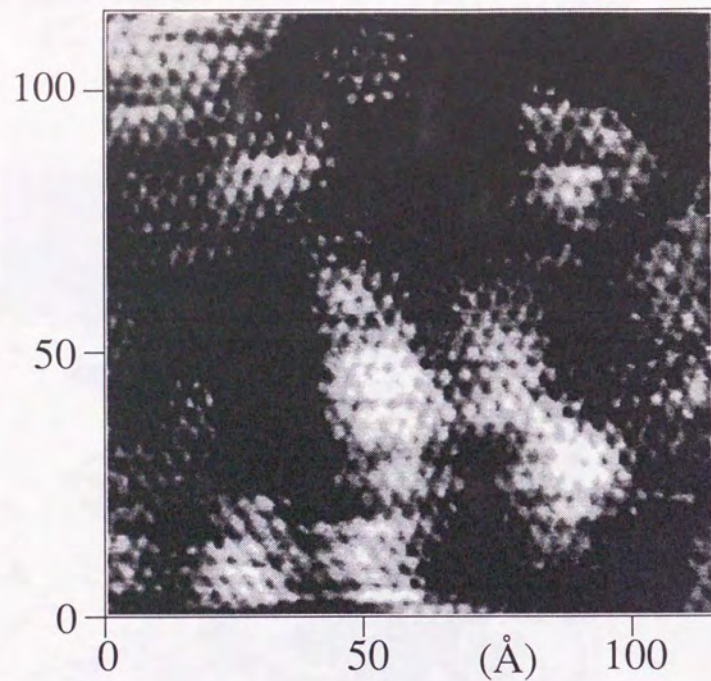
Fig. 4-4-1: A STM image of a 5ML L-film grown on MoTe2.

Intensity (arb.units)

(b) 160K

(a) 360K

(c)

24          23          22

Binding Energy (eV)
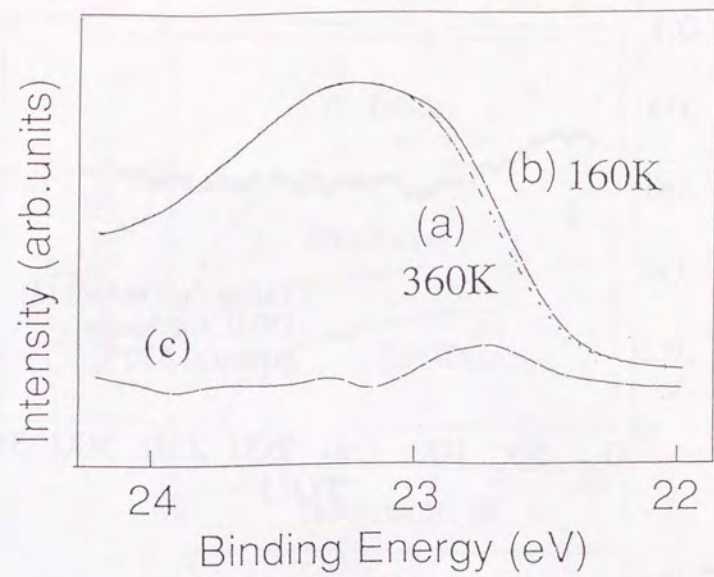
Fig. 4-4-2: Temperature dependence of XPS Ta($4f_{7/2}$) core levels of L-films. (a) 360K , (b) 160K , (c) a subtraction spectrum (b)-(a).
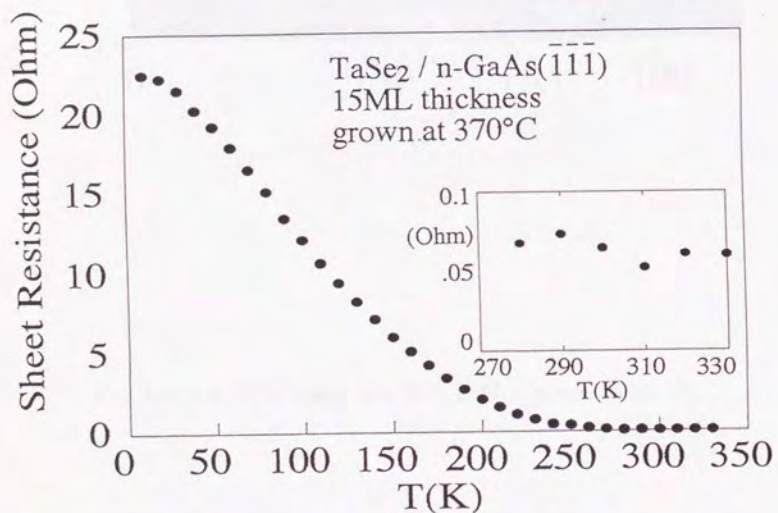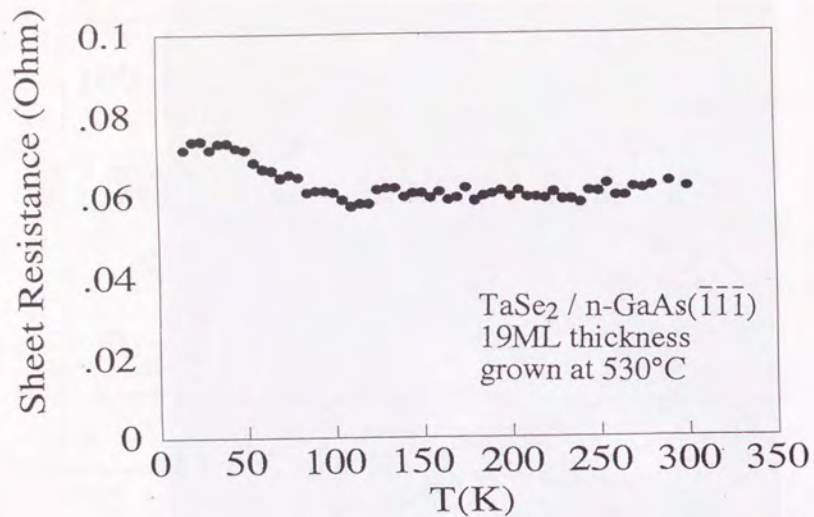
Fig. 4-4-3: Temperature dependence of the resistivity of TaSe$_2$ films grown on Se-terminated n-type GaAs($\overline{1}\overline{1}\overline{1}$) surfaces. The electric current flowing in the substrates was negligible. (Resistivity > 100 kΩ at 295K.)
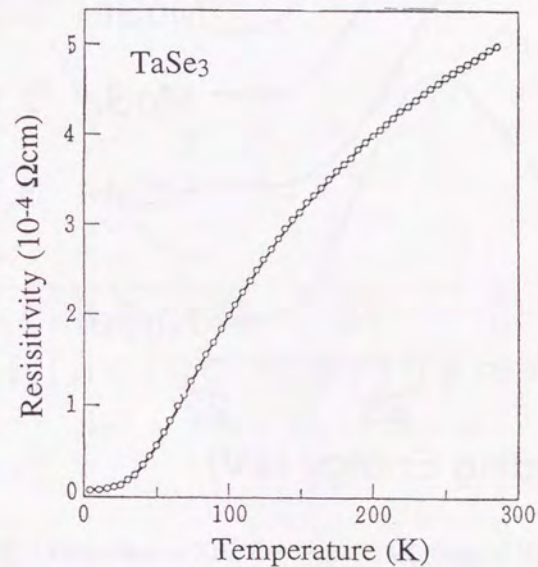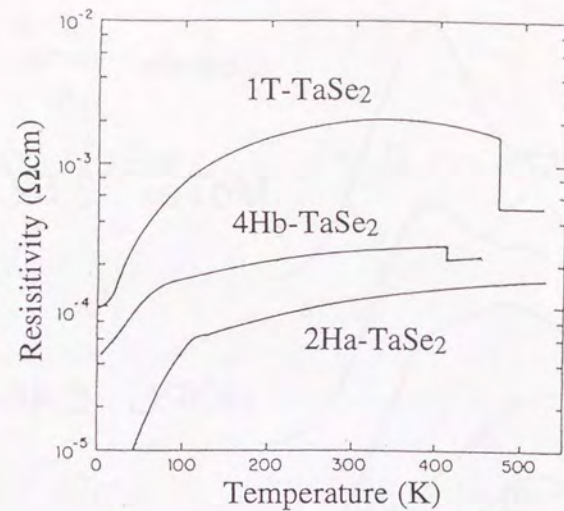


Fig. 4-4-4: Resistivity of TaSe2 [14b] and TaSe3 [14c].

| substrate | lattice const. (Å) | work func. (eV) |
|-----------|----------|----------|
| MoTe₂ | 3.52 | 4.1 |
| HOPG | 2.46 | 4.5 |
| MoSe₂ | 3.29 | 4.4 |
| MoS₂ | 3.16 | 4.8 |
| HfSe₂ | 3.75 | 4.9 |
| NbSe₂ | 3.45 | 5.9 |
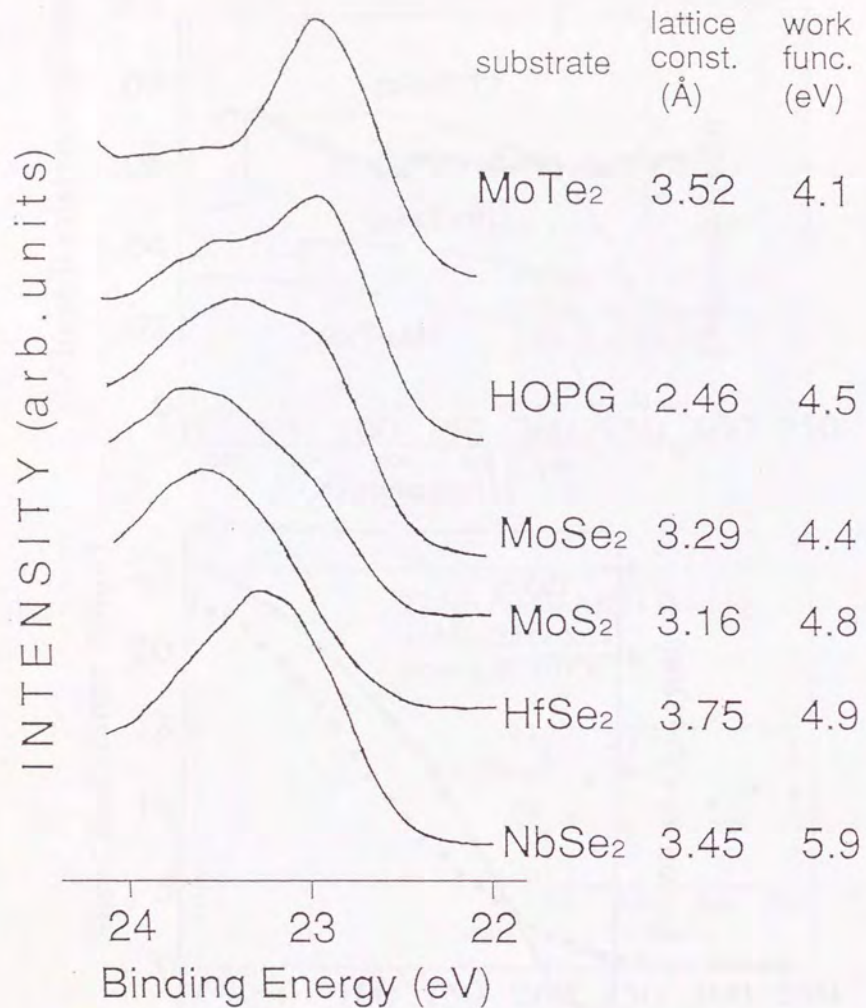
Fig. 4-5-1: XPS Ta(4f$_{7/2}$) core levels of 1ML L-films grown on various layered substrates.
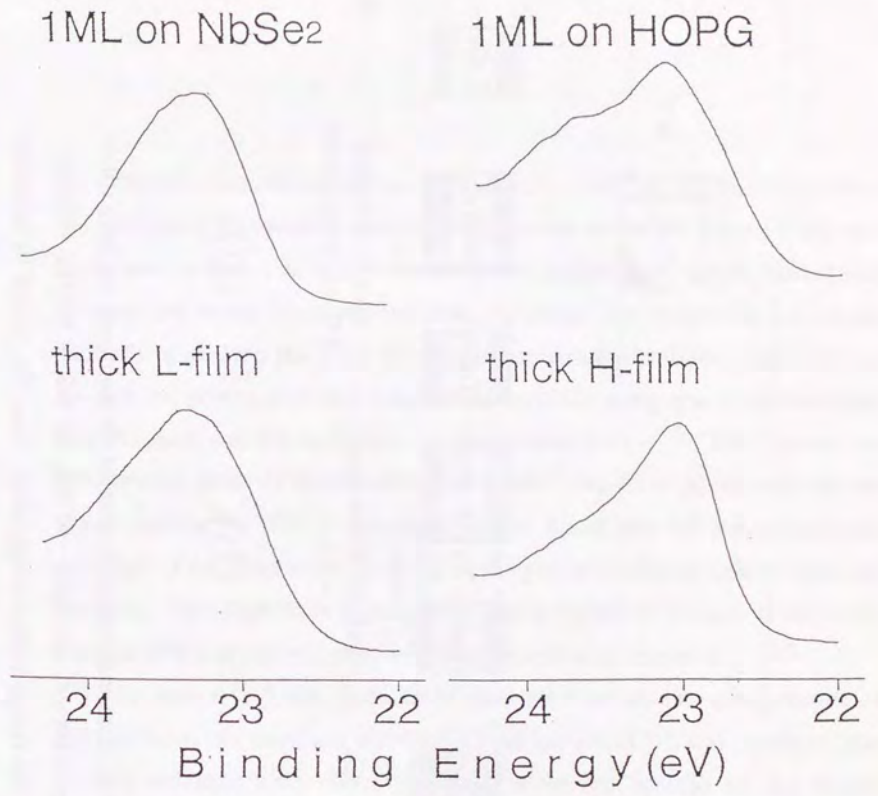


Fig. 4-5-2: Comparison of XPS Ta(4f$_{7/2}$) of 1ML films of NbSe₂ and HOPG substrates with thick films. The S(2p$_{3/2}$) peak positions were 161.2 eV for 1ML films on NbSe₂ and thick L-films, and 161.5 eV for 1ML films on HOPG and thick H-films, respectively.
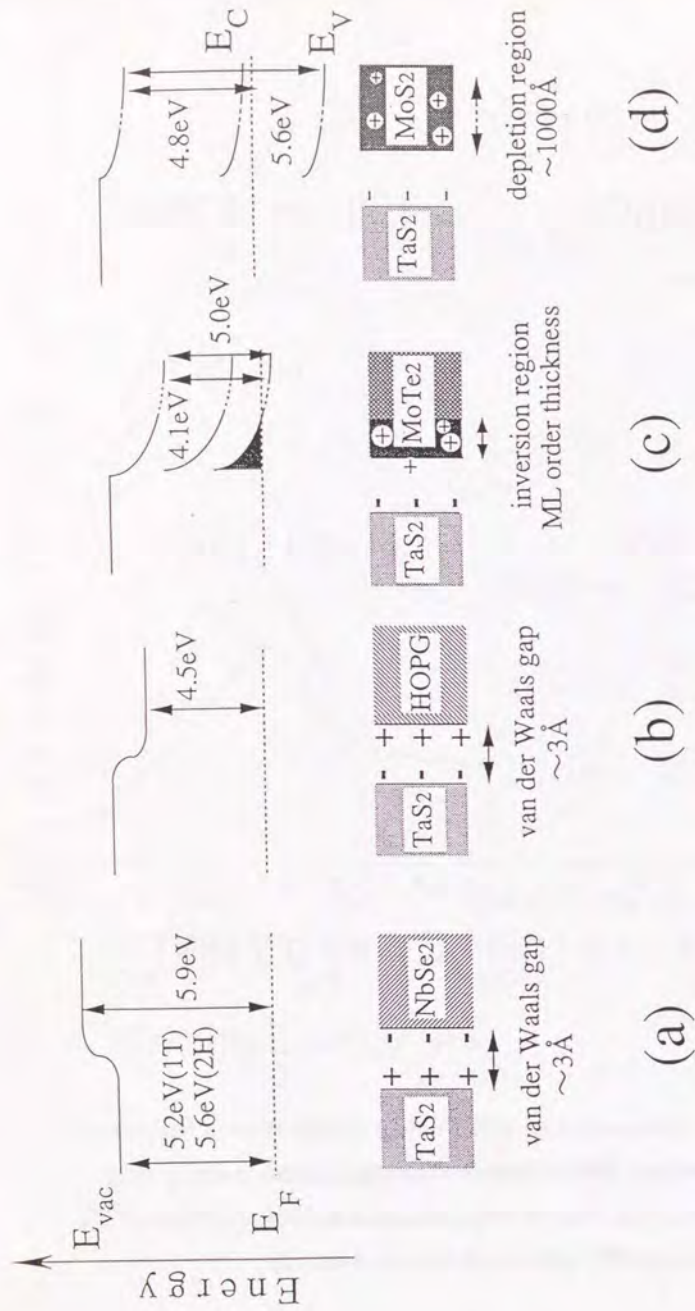
Fig. 4-5-3: Schematic energy diagram of the interfaces: (a) TaS$_2$ (film) - NbSe$_2$ (substrate), (b) TaS$_2$ - HOPG, (c) TaS$_2$ - MoTe$_2$, (d)TaS$_2$ - MoS$_2$. The energy scale is exaggerated. $E_{vac}$, $E_F$, $E_C$ and $E_V$ represent the vacuum level, Fermi level, conduction band minimum and valence band maximum, respectively.

# Chapter 5. Three dimensional structure determination of ultrathin films fabricated by van der Waals epitaxy using grazing incidence x-ray diffraction

As seen from the discussion in the preceding chapters, the determination of the polytype of the ultrathin films fabricated by van der Waals epitaxy is essential to the present study. It is therefore desired to analyze three dimensional atomic arrangement in the films with nm-order thickness. By comparing the various methods to analyze the three dimensional structure of ultrathin films, it was decided that grazing incidence x-ray diffraction (GID) using synchrotron radiation was the most suitable technique for the present study. In this chapter, the experimental study of the ultrathin NbSe$_2$ and TaSe$_2$ films grown with van der Waals epitaxy by GID is described. It was found that the crystallographic polytypes of the films were dependent on the growth conditions and the substrate materials. The temperature dependence of the polytype of TaSe$_2$ was consistent with the XPS analysis of 5 monolayer films described in chapter 4.

In section 5-2, the methods to determine the atomic arrangements of ultrathin films and interfaces are reviewed and compared. It was concluded that grazing incidence x-ray diffraction (GID) is the best method for the present purpose. The principle of GID is explained in section 5-3. In section 5-4, an experimental study on the ultrathin NbSe$_2$ and TaSe$_2$ films grown with van der Waals epitaxy by GID is described. It was found that the crystallographic polytypes of the films dependent on the growth conditions and the substrate materials.

## 5-1. Introduction

As seen from the discussion in the preceding chapters, the determination of the polytype of the ultrathin films fabricated with VDWE is essential to the present study. It is therefore desired to analyze three dimensional atomic arrangement of films with nm-order thickness. Among the layered materials fabricated by VDWE, NbSe$_2$ and TaSe$_2$ have drawn a wide attention in solid state physics because of their low dimensionality and strong electron phonon interaction. These characteristics have lead to unique phenomena represented by charge density waves and anisotropic superconductivity. Although the polytypes of TaS$_2$ and TaSe$_2$ films were determined in chapter 4 using characteristic Ta(4f) core levels, this method is not applicable to other materials. Structure analysis by commonly-used diffraction technique is applied in this chapter.

## 5-2. Structure determination of ultrathin films

The aim of this section is to review and compare the methods to determine the three dimensional atomic arrangement in ultrathin films. Electron diffraction techniques, electron emission holography, and x-ray diffraction are described. The conclusion is that grazing incidence x-ray diffraction has advantages over other method.

### 5-2-1 Low energy electron diffraction (LEED)

In LEED, an electron beam with a low kinetic energy (50 ~ 300 eV) is incident on the specimen surface at angle normal usually, and the spatial distribution of the diffracted electrons is measured by a phosphor screen or electron detector [1]. Since the mean free path of the electrons with those energy is the order of some Å, LEED is sensitive to the top most layers of the surface. LEED is generally used in the following two ways. One is two dimensional analysis, in which the diffraction pattern is used to analyze the structure of two dimensional unit cell of the surface. The other is three dimensional analysis by

elaborate calculation of the incident voltage dependence of the diffraction intensity. The intensity of each diffraction spot is determined by the relationship between three dimensional atomic arrangement inside the unit cell and the wavelength of the incident electrons. When the incident voltage is altered, the intensity of each spot changes differently. By analyzing the intensity-voltage (I-V) relationship, it is possible to estimate the three dimensional structure of the surface and sub-surface within about 1nm depth from the top surface. This technique has been used for the determination of well-defined structures such as surface recombination of silicon caused by adsorption. However, the procedure is on the try-and-error basis, i.e., making models and calculating the I-V characteristics, and comparing them with the experimental results. The calculation is complicated because the multi-scattering of electrons are strongly involved for the low incident energies. It actually applies procedures similar to band calculation because the low energy electrons travel in the sample just in the same manner with the electrons consisting energy bands. Consequently, the calculation is very cumbersome and some approximation is usually used because quick convergence cannot be expected in the try-and-error analysis.

With this background, an LEED analogue of the electron emission holography is proposed recently by several groups [2]. However, it is only applicable to simple systems in which not many atomic species exist in the specimen. These methods related with LEED were not utilized in the present work for the above reasons.

### 5-2-2 Reflection high energy electron diffraction (RHEED)

A high energy electron beam (10 ~ 30 keV) impinged with a grazing incidence (~1°) to the surface is diffracted in RHEED [3]. Although the mean free path of the high energy electrons is about 10 ~ 100 nm, since the penetration depth is proportional to the sine of the incident angle, this technique is also surface sensitive. The diffraction pattern from the smooth surface of single crystals

consists of elongated spots or streaks. These patterns can be interpreted as the intersections of the Ewald sphere and the rod-structured reciprocal lattice (Bragg rods). Ewald sphere and Bragg rods represent the conservation of the energy and momentum, respectively (Fig. 2-3-1). Although the momentum conservation perpendicular to the surface is not strict as seen from the elongation along this direction, it is weakly reflected to the diffraction pattern. This can be utilized for the analysis of the three dimensional structure. It requires the measurement of the intensity profile as a function of momentum transfer perpendicular to the surface. One must control the sample azimuth precisely in order to change the crossing points of the Bragg rod and the Ewald sphere, which is difficult without a sophisticated goniometer. This method also has a problem of the multi-scattering of the electrons, which leads to ambiguity of the analysis.

### 5-2-3 Electron emission holography

Recently, a method to analyze the angle resolved photoemission or Auger electron diffraction as a modified holography is invented [4]. This method can be used to reconstruct three dimensional image around certain atomic species. This is a direct method without using model calculations because the multi-scattering and phase shift can be neglected or compensated. However, the effects of inhomogenious source wave and diffraction are not totally negligible and cumbersome calculation is needed for precise determination of atomic positions.

### 5-2-4 Grazing incidence x-ray diffraction (GID)

This method, utilizing strong x-ray from synchrotron radiation, is a promising method for the three dimension structural analysis of surface and ultrathin films. The principle of the method is described in the following section. Although comparison with model calculations is involved, the calculation can be performed within the single scattering or kinematical scheme in contrast with the electron diffraction techniques.

### 5-3. Principle of grazing incidence x-ray diffraction (GID)

The merit of using x-ray diffraction for the structure analysis is that the weak interaction of x-ray with materials allows the application of simple single scattering (or kinematical) approach for ordinary crystals. Owing to the development of strong synchrotron radiation (SR) sources, x-ray diffraction has been introduced to surface science as a promising characterization tool of surfaces in 1980s [5,6]. Since SR is stronger than ordinary x-ray tube sources by more than three or four orders of magnitudes, the smallness of the amount of scatters at surfaces is compensated in principle. The problem for the surface measurement comes from the background due to the substrates. In this context, GID technique has been studied and has made a success in determining three dimensional structure of surfaces, adsorbates and ultrathin films such as Langmuir-Blodgett films. In the following, I will make a brief review on the principle of the grazing incidence x-ray diffraction for the surface analysis according to [5].

The refraction index (n) of x-ray for a material is almost determined only by the electron density because the energies of interband or core level excitations are much lower than the x-ray energy (4~10keV) except for the most inner core levels. It can be written as:

$$n = 1 - \frac{\lambda^2 e^2 F(0)}{2\pi mc^2 V} \equiv 1 - \delta, \qquad (5-4-1)$$

where $\lambda$ is the wavelength of the x-ray, $F(0)$ is the structure factor at zero momentum transfer, c is the velocity of light, e and m are the charge and mass of electrons, respectively, and V is the volume of the unit cell.

Since $n < 1$, total refraction of the incident beam occurs at the critical angle ($\alpha_c$) which is defined as $\cos \alpha_c = n$. Here the incident and exit angles are measured from the surface plane. For small angles, $\alpha_c \simeq \sqrt{2\delta}$ which is of the order of $0.1°$ to $1°$ for ordinary materials and $\alpha_c$ is an increasing function of the electron

density. The penetration depth ($\Lambda$) of x-ray for the incident angle ($\alpha_i$) smaller than the critical angle is written as

$$\Lambda = \frac{\lambda}{4\pi}(\alpha_c{}^2 - \alpha_i{}^2)^{-1/2}. \qquad (5\text{-}4\text{-}2)$$

However, $\Lambda$ cannot be smaller than $\Lambda_{min} = \lambda / (4\pi\,\alpha_c)$ which is several nm for the ordinary materials. We can see from eqs. (5-4-1) and (5-4-2) with the relation $\alpha_c \simeq \sqrt{2\delta} \propto \lambda$ that the minimum $\Lambda$ ($\Lambda_{min}$) is not dependent on $\lambda$. Values of $\Lambda_{min}$ are 51, 32 and 12 Å for water, Si and Au, respectively. This small penetration depth will make the background coming from the substrate small enough for the measurement of the surfaces. This probing depth is longer than that of the electron diffraction techniques. It is suitable for the polytype analysis of the layered materials because the length of the unit cell perpendicular to the surface is 6 (1T) ~37 (6R) Å, which can be smaller than the penetration depth. Nevertheless, it must be noted that GID is hardly applicable to the case in which the lattice constant of the film is too close with that of the substrate.

Next we proceed to the enhancement of the surface scattering due to standing wave phenomenon. The reflectivity (R) is given from the Fresnel equation (related to boundary condition) as

$$R = (\alpha_i - \alpha_i') / (\alpha_i + \alpha_i'), \qquad (5\text{-}4\text{-}3)$$

where $\alpha_i' = (\alpha_i{}^2 - \alpha_c{}^2)^{1/2}$ is the penetration angle of x-ray measured from the surface plane. R takes maximum value of 1 when $\alpha_i = \alpha_c$, which means the field strength at the surface is twice of the incident beam. This is interpreted as due to the standing wave at the surface. It leads to the enhancement of the surface diffraction by the factor of 4 ($=2^2$), if the absorption and irregular scattering can be neglected. It should be noted that the signal to noise ratio in GID is determined by the competition between the reduction of the substrate signal and the enhancement of the surface signal, in which the former is far more important than the latter. Since there is a minimum penetration depth determined only by the materials irrelevant to the incident angle and the wavelength of x-ray, there are some limitations in the surface measurement which are summarized as follows:

(i) The in-plane lattice constant of the specimen (surfaces, adsorbates, and films) must be different from that of the substrate. The measurable samples are, therefore, reconstructed surface, non 1x1 adsorbates, and epitaxial films with different lattice constant with the substrate.

(ii) Surface roughness must be avoided as much as possible, because it causes the smearing of Bragg rod profiles and enlarges the background from the substrate.

In the experiment described below, heteroepitaxial films with 3 ~ 9 nm thickness were successfully measured with GID. The monolayer systems treated in section 4-3 ($TaS_2$, $TaSe_2$ / HOPG and $TaS_2$, $TaSe_2$ / $NbSe_2$) could not be measured because of the small thickness and the close lattice constant between the film and the substrates (e.g. 0.345 and 0.343 nm).

## 5-4. Structure determination of ultrathin films of layered materials by GID

### 5-4-1 Introductory remark

In this section, I report the determination of the structures of $NbSe_2$ and $TaSe_2$ films grown at various temperatures on HOPG and GaAs($\bar{1}\bar{1}\bar{1}$) substrates by GID. The polytypes of these layered materials have importance in the study of the physical properties of the VDWE-grown films as well as a pure scientific interest for the mechanism of polytypism. The experiment at the photon factory, KEK, has revealed that the polytypes of the films were dependent on the growth temperature and the substrate materials.

### 5-4-2 Model calculations - feasibility of polytype determination by GID

Since the in-plane lattice spacings of $NbSe_2$ and $TaSe_2$ are not sensitively dependent on polytypes as shown in Table 5-4-1, it is hardly possible to distinguish one polytype from others just by measuring the in-plane lattice spacings. Neither can 00n reflections (n: index perpendicular to the layer) be used for the present purpose because they will give only one type of intensity

distribution independent of the polytypes due to the symmetry of the crystals. It can, however, be expected to distinguish these by measuring the Bragg rod profile which reflects the structure normal to the surface. We have calculated Bragg rod profiles for all of the polytypes of $NbSe_2$ found in the literature [7]. The calculations were performed according to the kinematical diffraction theory [5] with the atomic scattering factors in a published table [8] and lattice parameters compiled by Wilson and Yoffe [6]. Figure 5-4-2 and -3 shows Bragg rod profiles for 10 reflection of 7 monolayer (ML) films for various polytypes of $NbSe_2$ and $TaSe_2$, respectively. When the thickness of the films was changed, the peak positions were maintained while the peak width was roughly inversely proportional to the thickness. Surface roughness and thermal vibrations were neglected in the calculation for Fig. 5-4-2 and -3, whereas 60° rotated twin crystals were taken into account in order to make the comparison with the experimental results. Instrumental function derived below is included in the calculation. Since substantial differences can be found among the simulations for the various polytypes, GID can be used to determine the polytypes.

### 5-4-3 Experiments

The ultrathin films of $NbSe_2$ and $TaSe_2$ were grown in a ultrahigh vacuum (UHV) chamber with a base pressure of $3 \times 10^{-8}$ Pa. Selenium was emitted from a Knudsen cell while niobium (99.95 % purity) and tantalum (99.99 % purity) were evaporated from electron bombardment sources. The typical sizes of the substrates were 8mm x 8mm and 5mm x 5mm for Se-GaAs and HOPG, respectively. GaAs(111) was cleaned and Se-terminated by heating at 590°C under Se atmosphere [9], whereas HOPG substrates were prepared by heating at 800°C under UHV condition after cleavage in the air.

The growth rates of $NbSe_2$ and $TaSe_2$ were of the order of 0.5 monolayer (ML) / min as measured by quartz oscillator thickness monitor. The substrate temperature was monitored with W-Re thermocouple and was maintained to a

constant value during the growth. Samples measured by GID were investigated with reflection high energy electron diffraction (RHEED) during the growth. The crystallinity and the flatness of the grown surfaces were confirmed by the sharp streak patterns without noticeable structures along the Bragg rods. The patterns from the films grown on Se-GaAs were with six-fold azimuthal symmetry while the films on HOPG exhibited columnar streaks, as expected from the symmetry of the substrates. The sample description is summarized in Table 5-4-4 with the experimental results.

After the growth, the samples were taken out to the ambient atmosphere, then sealed in Pyrex tubes evacuated to $1 \times 10^{-3}$ Pa and transferred to a 53-pole permanent magnet wiggler beam line (BL-16X) at the Photon Factory [10]. The diffractometer set up in the present experiment was the same one that had been used in the study of monolayer films on water surface [11]. The wavelength of the x-ray beam was determined to be $0.902 \pm 0.003$ Å from the diffraction peaks of a GaAs single crystal. The x-ray beam was focused horizontally by a sagittal focusing Si(111) double crystal monochromator, then reflected downward and vertically focused by a bent platinum-coated fused quartz mirror. The glancing angle of the x-ray beam to the surface of the specimen was 1.8 mrad. Samples sealed in the evacuated Pyrex tubes were taken out to the ambient atmosphere and mounted horizontally on the two-circle diffractometer. The diffracted x-ray intensity was measured by a one dimensional position sensitive proportional counter (PSPC) through a Soller collimator. They were mounted on the $2\theta$-arm of the diffractometer. The Soller collimator had an angular resolution of 0.1° in the horizontal plane and covered an angular range of -3.7° to 13.4° along the surface normal, which corresponds to the range of -0.45 Å$^{-1}$ to 1.65 Å$^{-1}$ in the reciprocal space. The overall nominal instrumental resolution in the horizontal plane was 0.17° and the measured width of the direct beam corresponded to $9.2 \pm 0.1 \times 10^{-3}$ Å$^{-1}$. In order to measure the background profile, an area of about 0.05 Å$^{-2}$ in the reciprocal space was scanned by rotating the detector (angle $\phi$) and the sample

(angle $\omega$) independently. The observed diffraction patterns did not change during the x-ray irradiation for several hours nor after one week interval in the ambient atmosphere. PSPC outputs at certain $\phi$ and $\omega$ were accumulated for 60 ~ 300 s, and a data set for one specimen was obtained in several hours.

### 5-4-4  Analysis of the diffraction data
#### A. Films on Se-GaAs

Diffraction corresponding to the lattice constants of the grown materials were observed with a tolerable signal to noise ratio in a few hours from the films thicker than 4ML. They had six-fold symmetry just as RHEED patterns did and intensity profile measured with PSPC did not make significant difference when the samples were rotated by 60°. Therefore we use the diffraction indexes 10 and 11 here neglecting 60° rotation. In order to illustrate the procedure of data processing, (10) rod of a $NbSe_2$ film with 7ML thickness grown on Se-GaAs at 500°C ($NbSe_2$ / Se-GaAs 500°C) is taken for example in the following. While the azimuth of the detector ($\phi$) was increased from 16.8° to 17.6°, the sample (angle $\omega$) was rotated by ±10° with a 0.25° step to make a rectangular mesh with 10 x 41 vertices in $\phi$–$\omega$ space. Figure 5-4-5 shows the 'cross sections' of the collected intensity profile for constant $q_z$ plane. Area with maximum intensity changes its position in the $\phi$–$\omega$ space for different $q_z$, which is due to the geometry in the reciprocal space. Figure 5-4-6 illustrates the relation of the Ewald sphere and a Bragg rod to explain this effect. As described in the review by Feidenhans'l [5], measurement at a finite $q_z$ requires crossing of the Bragg rod with Ewald sphere at corresponding $q_z$. Therefore $\omega$ and $\phi$ for the Bragg rod center changes with $q_z$. The transformation from ($\omega$, $\phi$, $q_z$) coordinates to reciprocal coordinates ($q_1$, $q_2$, $q_z$) is performed by the following formula:

$q_1 = q_{//} \cos(\theta - \omega)$,  $q_2 = q_{//} \sin(\theta - \omega)$,

where $q_{//} = k \sqrt{(\cos\alpha_f \cos\phi - \cos\alpha_i)^2 + (\cos\alpha_f \sin\phi)^2}$ ,

$$\theta = \tan^{-1}\left(\frac{\cos\alpha_i - \cos\alpha_f \cos\phi}{\cos\alpha_f \sin\phi}\right) ,$$

and  $\alpha_f = \sin^{-1}\left(\frac{q_z}{k} - \sin\alpha_i\right)$.  (5-4-4)

The scans in Fig. 5-4-5 are transformed into reciprocal space according to this formula and shown in the insets. The Jacobian of transformation eq.(5-4-4) is

$dq_1 dq_2 = 2 k^2 \cos\alpha_i \sin\phi / 4\pi^2 A \, d\omega \, d\phi$ ,  (5-4-5)

where A is the area of the surface unit cell.

The factor $\sin\phi$, therefore, was multiplied to the raw intensity data in the following intensity analyses.

As seen from Fig. 5-4-5, considerable backgrounds were observed in the measured data. Hence certain areas in $\phi$–$\omega$ space outside the Bragg rod were chosen to estimate the background (Fig. 5-4-5). For every step of $q_z$, averaged intensity of the area was subtracted from the total summation over the scanned area to calculate Bragg rod profile. The result is shown in Fig. 5-4-7 with 11 rod profile analyzed by similar procedure. The shapes of the Bragg rods in the reciprocal space were obtained by converting ($\omega$,$\phi$) scan to the reciprocal coordinates and taking summation over measured $q_z$. They are shown in the insets by the contours at 100%, 80%, 50%, 30% of the maximum. The abscissa ($q_x$) were taken so that the lines determined by $q_x=0$ represent the directions of the principal axes of the GaAs substrate. The alignment of the axes of the film and the substrate is confirmed by the position of the Bragg rod maximum. The full width at half maximum (FWHM) of the Bragg rod along the axis was $3.7 \times 10^{-2}$ Å$^{-1}$, while that of the direct beam was $9.2 \times 10^{-3}$ Å. The in-plane lattice constant was determined to be $3.46 \pm 0.01$ Å from the peak position in the reciprocal space, which is consistent to the value for bulk $NbSe_2$ (3.45Å) within error.

The effect of finite size of the samples was not negligible in the present experiment. The angle of elevation from the sample to a certain channel of the PSPC changes with the position on the sample. Because of this effect the intensity at $q_z$ becomes a convoluted value as following:

$$I(q_z) = \int_{sample} g(k(\sin\alpha_i + \sin\alpha_f(x))\ dx\ dy,$$

$$\text{and } \alpha_f(x) = \tan^{-1}\left(\frac{L}{L-x}\tan(\sin^{-1}(\frac{q_z}{k} - \sin\alpha_i)))\right), \tag{5-4-6}$$

where $q_z$ is the value for the center of the sample (O); $g(q_z)$ is the true Bragg rod profile; L is the distance between the center of the sample and the point at which PSPC crosses the surface plane ($P_0$); x, y are Cartesian coordinates on the sample surface which is taken so that x-axis is a vector from point O to point $P_0$; the integral is performed on the sample surface area. Since the deconvolution of eq. (5-4-6) deteriorates the signal to noise ratio of the Bragg rod profile, eq. (5-4-6) is instead operated on the result of the model calculation and the results are compared with the experimental data.

B. Films on HOPG

The diffraction patterns from NbSe$_2$ / HOPG did not change by rotating the sample. It was due to the structure of the HOPG substrate which consists of graphite microcrystals aligned only along c-axis. Shown in Fig. 5-4-8 are the intensity profile corresponding to the 10 rod of a NbSe$_2$ / HOPG for different detector azimuth ($\phi$). As seen from the figure the intensity at higher $q_z$ decreases with $\phi$. This also comes from the geometry in the reciprocal space, in which Bragg rods from the rotated crystals form coaxial cylinders. The fact that the diffracted intensity is not zero for a certain range of $\phi$ indicates that the Bragg rod has a measurable broadness. In order to estimate it, we assume Gaussian distribution of the in-plane Bragg rod intensity as follows:

$$I(q_z, d) = g(q_z)\exp(-t\,d^2), \tag{5-4-7}$$

where $g(q_z)$ is the true Bragg rod profile to be obtained, and

$$d \equiv d(\omega)$$
$$= ((q_{//}\cos\omega + k\cos\alpha_i - (k^2 - q_z^2)^{1/2}\cos\phi)^2 + (q_{//}\sin\omega - (k^2 - q_z^2)^{1/2}\sin\phi)^2)^{1/2}$$

is the distance between the point ($\omega$, $\phi$, $q_z$) and the center of the Bragg rod.

Using eq.(5-4-7) the diffraction intensity from the cylindrical Bragg rod is

$$G(q_z) = g(q_z)\int_0^{2\pi} \exp(-td(\omega)^2)\ d\omega, \tag{5-4-8}$$

$$\text{or}\quad g(q_z) = G(q_z)\Big/\int_0^{2\pi} \exp(-td(\omega)^2)\ d\omega, \tag{5-4-8'}$$

where $G(q_z)$'s for different $\phi$ have been measured experimentally.

We derived $g(q_z)$ from $G(q_z)$ through making the combination of $q_{//}$ and t which yield the least dependence of $g(q_z)$ on $\phi$ after the calculation of eq. (5-4-8'). After numerical computing, we obtained $q_{//}$=2.08 $\pm$ 0.01 Å$^{-1}$ and t = 2500 $\pm$ 500 Å. The in-plane lattice constant was calculated from $q_{//}$ as 3.50 $\pm$ 0.01 Å, of which difference from the bulk value is less than 2%. From the value for t , the FWHM in the broadness of (10) rod is calculated to be 1.7$\pm$0.3 x 10$^{-2}$ Å$^{-1}$. After the subtraction of the direct beam width, genuine peak width is obtained as 7.7 $\pm$ 4 x 10$^{-3}$ Å$^{-1}$. Figure 5-4-8 shows the determined $g(q_z)$ for the same $\phi$ values as broken lines, in which one can see the agreement of $g(q_z)$'s is excellent. The residual differences in the profile are probably due to the warping of the HOPG substrates. The $g(q_z)$ profiles in Fig.5-4-8 (b)-(d) were averaged to obtain a good signal to noise ratio for the wide range of $q_z$. The result is shown in Fig. 5-4-11 (a) as a dotted curve.

*5-4-5 Results*

Dependence of the Bragg rod profile on the substrate temperature of TaSe$_2$ and NbSe$_2$ films on Se-GaAs is shown as dotted curves in Figs. 5-4-9 and -10, respectively. Systematic differences in the both materials are clearly observed. The deviation of the in-plane lattice constant of the films was less than 2%. In order to investigate the substrate effect separated from other factors, NbSe$_2$ films shown in Figs. 5-4-11(c) (same as Fig. 5-4-10(c)) and 5-4-11(a) were fabricated under the same growth condition. The difference is easily recognized.

### 5-4-6 *Comparison of experimental results with simulations*

The structures of the films were investigated by comparing the experimental Bragg rod profile with kinematical simulations. Since the simulation was dependent on the selection of the top-most layer because of the finite thickness of the film and the small penetration of x-ray, all the combinations were summed over in the simulation. The simulations of 60° rotated twins were also added up because the experimental results did not show the difference with 60° rotation. Then the results showing the most similar features with the experiments were chosen for the further analyses. After the polytype and the thickness was determined, Debye-Waller factors along c-axis are calculated by the least-square fitting with taking the apparatus function (eq.(5-4-6)) into consideration. For the experimental results which cannot be explained by a single polytype, mixture of the polytypes were considered. Since some experimental Bragg rod profile showed smearing of the fine structure, disorders, i.e., deviation of the layer spacing and the corrugation of the layers were taken into account. The results are shown in Figs. 5-4-9 ~ -11 as solid lines. The determined polytypes and the in-plane widths (FWHM) of 10 Bragg rods, which is related with the domain size of the films, are summarized in Table 5-4-4. The calculations for 11 rods, which did not make the noticeable difference by changing the polytypes, were in good agreement with the experimental results.

### 5-4-7 *Temperature Dependence of TaSe$_2$*

The temperature dependence of the polytypes of TaSe$_2$ films shows good agreement with XPS and STM analysis in chapter 4. However, it is different from the condition for the bulk crystal growth. In the bulk growth by vapor transport, it is established that 1T is the high temperature form only stable above ~800°C [12] while the most stable form below ~300°C is 2Ha. However, the temperature dependence in VDWE is different from above, which is probably due to the non-equilibrium nature of MBE.

Although different kinds of experiments are needed to discuss the precise mechanism for our observation, it is speculated in the following. Ta atoms are octahedrally (OC) coordinated in 1T-polytype whereas they are coordinated in trigonal prism (TP) in 2Ha-polytype. The stability of these coordinations have been studied in molecular complexes of transition metals [13]. The result of the analysis using ligand field theory was, in brief, that OC is not less stable than TP in the complexes containing only one metal atom. I here associate this theory with the mechanism of VDWE. If the reaction of Ta with Se in molecular species takes place before the crystallization of the film, the factor determining the polytype can be the ligand field stabilization energy in the molecule, which favors the OC-coordination (1T). While at low substrate temperature these clusters will crystallize without changing the coordination, at higher temperature they will move around and probably change their structures on the surface until settling at the most energetically favorable form as a bulk crystal (2Ha). Namely, small clusters of TaSe$_2$ are "quenched" at low substrate temperatures. This model explains the present observation that 1T and 2Ha are formed at lower and higher temperatures, respectively.

XPS measurement of TaSe$_2$ films grown below 420°C have shown a systematic change in Ta (4f) core level associated with the change of the temperature, substrate and thickness and anomaly in the resistivity (chapter 4) both of which suggests the occurrence of CDW. This is consistent with the present result that the polytype of TaSe$_2$ grown at 420°C was mainly 1T which is known to exhibit more prominent CDW than other polytypes.

### 5-4-8 *NbSe$_2$*

It was shown in the present experiment that polytypes of NbSe$_2$ are controlled by the substrate materials and growth temperature. First the temperature dependence is examined. At the temperature lower than and equal to 500°C, 2Hb and mixture of 2Hb and 3R is formed on the both substrate. They are

known as rare forms of NbSe$_2$ in the bulk. As for the mechanism of the formation of these particular polytypes, the role of surplus Nb at interstitial sites is suspected. It has been reported by Huisman et al. [12] that 3R and 2Hb- NbSe$_2$ have surplus Nb at interstitial sites as indicated by the formula Nb$_{1+x}$Se$_2$ where 0.05<x<0.15. Their result also indicates that 3R has more Nb than 2Hb. As seen from the fact that disorders had to be considered in the analysis of NbSe$_2$ on Se-GaAs, the crystallinity of the films on HOPG is better than that on Se-GaAs. We consider that the amount of interstitial Nb is larger in the films on Se-GaAs than those on HOPG and that the surplus Nb deteriorates the crystal order and makes the 3R-type on Se-GaAs substrates. The difference of the peak width of the 10 diffraction, 2.8±0.3 x 10$^{-2}$ Å$^{-1}$ and 7.7± 4 x 10$^{-3}$ Å$^{-1}$ for the films on Se-GaAs and HOPG grown at 500°C, respectively, is also consistent to this explanation. Since the 2Ha-type formed at 535°C on Se-GaAs, the interstitial Nb is less at higher growth temperature which is near to the ordinary bulk growth temperature (700 ~ 900 °C).

Next the substrate dependence is discussed. It is well known that migration and crystallization on the substrate surface are important for the molecular beam epitaxy [14]. The present result seems to indicate that these processes are not the same on different substrates. The mechanism will be one of the followings: (i) difference in the van der Waals interaction between the growing film and the substrate, (ii) difference in microscopic morphology of the substrate surfaces, and (iii) different stable precursors for the crystallization.

## 5-5. Conclusion and outlook

Grazing incidence x-ray diffraction technique was applied to analyze the three dimensional structure of epitaxial films of NbSe$_2$ and TaSe$_2$ with nm-order thickness. The structures were dependent on the substrates and the growth temperature, which indicates the polytype was controlled by those conditions. As for TaSe$_2$ films, 1T-polytype was formed at lower growth temperature, which is different from the bulk growth conditions. This result verifies the XPS characterization of 5ML films in chapter 4. The temperature dependence might indicate that the molecular species of TaSe$_x$ is formed prior to the crystallization. From NbSe$_2$ films only 3R and 2Hb polytypes were observed, which is consistent with the former measurement of the physical properties of the films. These results will be useful to elucidate the mechanism of the epitaxy via van der Waals forces and to pursue novel physical properties in layered heteroepitaxial systems.

**Table 5-4-1:** Lattice constants of polytypes of TaSe₂ and NbSe₂.
'a' and 'c/n' denote the in-plane lattice constant and layer spacings, respectively.

| TaSe₂ polytype | 1T | 2Ha | 3R | 4Ha | 4Hb | 4Hc | 6R |
|---|---|---|---|---|---|---|---|
| a (Å) | 3.4769 | 3.436 | 3.4348 | 3.4362 | 3.4575 | 3.436 | 3.4558 |
| c/n (Å) | 6.2722 | 6.348 | 6.392 | 6.350 | 6.286 | 6.383 | 6.304 |

| NbSe₂ polytype | 1T | 2Ha | 2Hb | 3R | 4Ha | 4Hd$_I$ | 4Hd$_{II}$ |
|---|---|---|---|---|---|---|---|
| a (Å) | 3.53 | 3.449 | 3.451~7 | 3.459 | 3.444 | | 3.48 |
| c/n (Å) | 6.29 | 6.499 | 6.285~65 | 6.256 | 6.3075 | | 6.3625 |

**Table 5-4-4:** Descriptions and summary of results of the samples measured in the present experiment.

| film / substrate | growth temperature | thickness | RESULT polytype | peak width (domain size) |
|---|---|---|---|---|
| TaSe₂ / Se-GaAs | 590°C | 15ML | 2Ha | (~100Å) |
|  | 495°C | 16ML | 2Ha |  |
|  | 410°C | 8ML | 1T |  |
| NbSe₂ / Se-GaAs | 535°C | 1ML | 2Ha | $2.8 \pm 0.3 \times 10^{-2}$ Å$^{-1}$ (225Å) |
|  | 500°C | 7ML | 2Hb+3R | − |
|  | 420°C | 8ML | 2Hb+3R | − |
| NbSe₂ / HOPG | 500°C | 7ML | 2Hb | $7.7 \pm 4 \times 10^{-3}$ Å$^{-1}$ (820Å) |
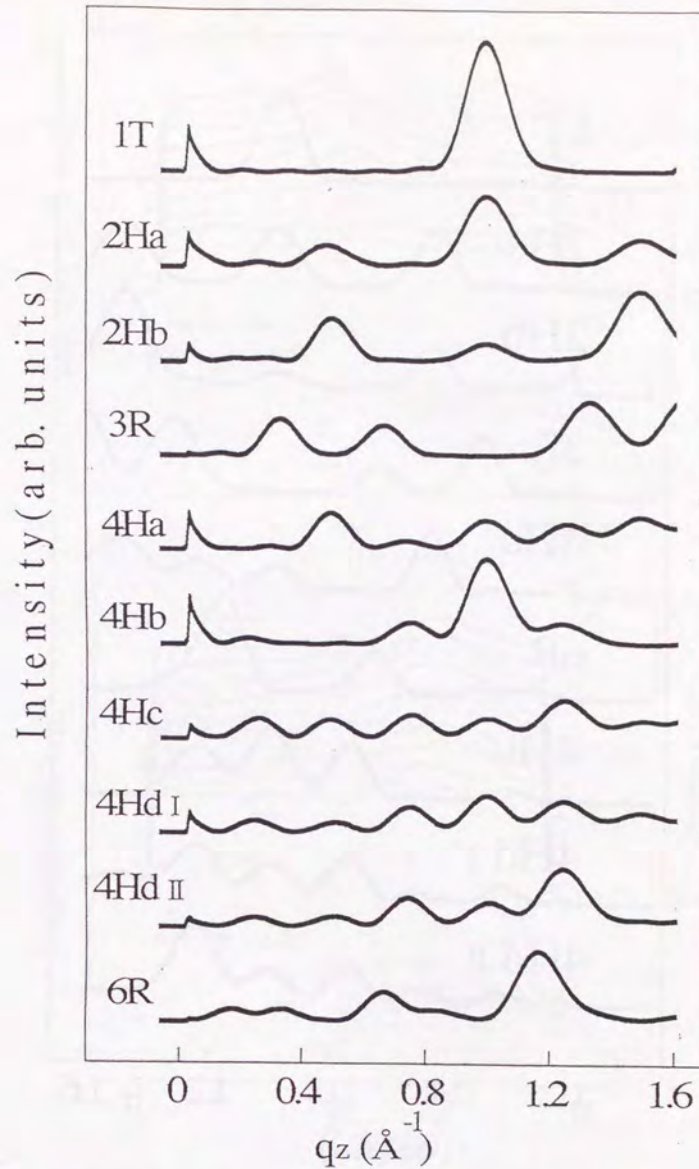
Fig. 5-4-2: Caluculated 10 Bragg rod profiles for TaSe₂ films with 7 ML thickness for various polytypes. No surface and lattice roughness are assumed whereas instrumental functions are taken into account.
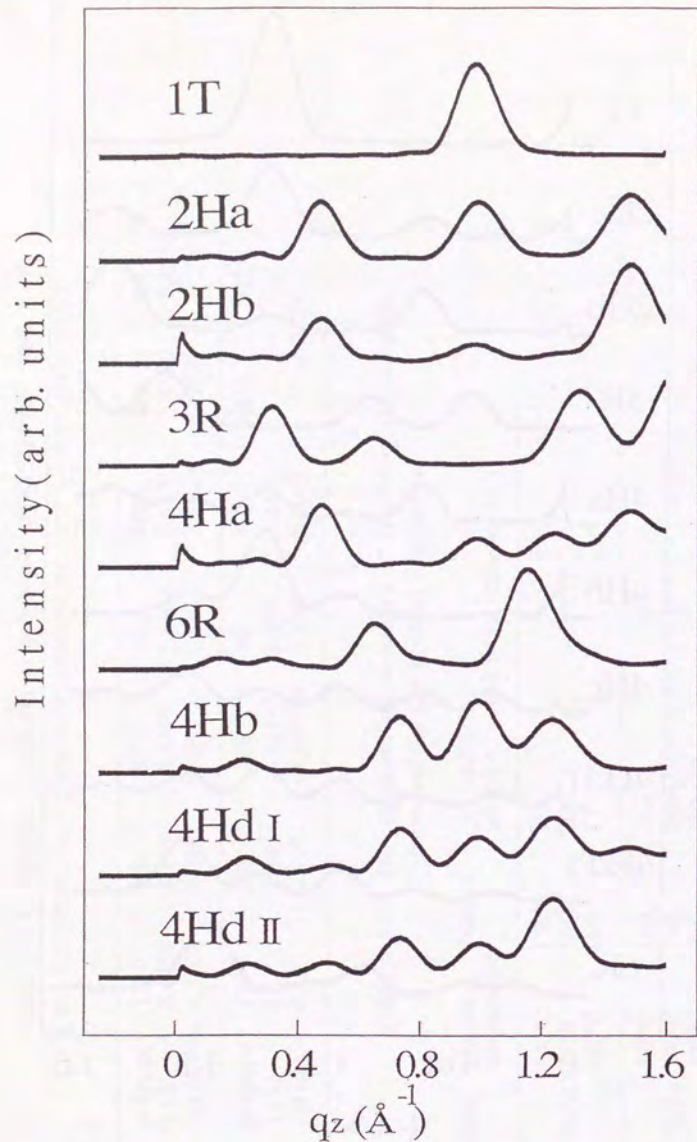
Fig. 5-4-3: Caluculated 10 Bragg rod profiles for NbSe$_2$ films with 7 ML thickness for various polytypes. No surface and lattice roughness are assumed whereas instrumental functions are taken into account.
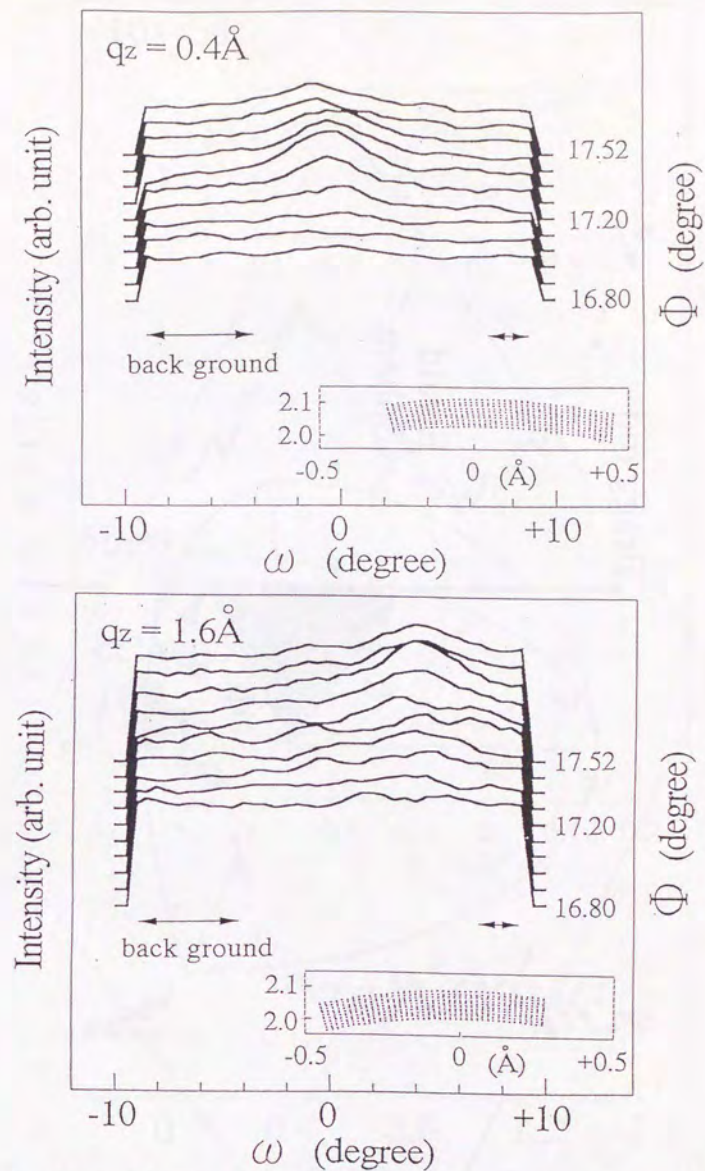


Fig. 5-4-5: Raw intensity data of the rod scan for 10 rod from a NbSe$_2$ film with 7ML thickness grown on Se-GaAs. $\phi$ is the detector azimuth and $\omega$ is the rotation angle of the sample. The area used for the background subtraction is also indicated with arrows. Insets show the relationship between $\phi-\omega$ scan and the reciprocal space. The dots indicate the measured points.
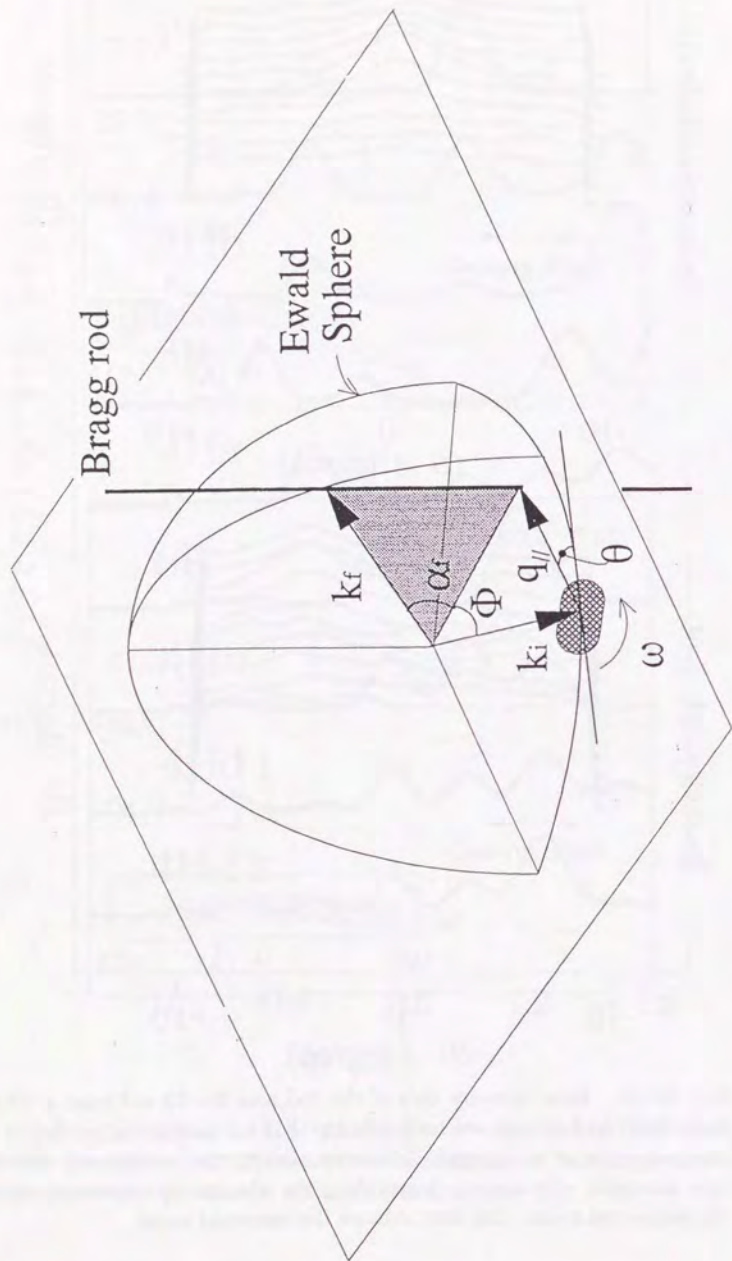
Fig. 5-4-6: Geometry in the reciprocal space. $\alpha_f$ is the exit angles of X-ray (incident angle $\alpha_i$ is ignored), $\phi$ and $\omega$ is the same as Fig. 5-4-5, $q_z$ and $q_{//}$ are the wavenumber of the transferred momentum perpendicular to and parallel with the surface, and k is the wavenumber of the X-ray.

Bragg rod

Ewald Sphere

$k_f$

$\alpha_f$

$\Phi$

$q_{//}$

$k_i$

$\theta$

$\omega$



(10) rod

80
50    30%

-0.2   -0.1   0   0.1   0.2
(Å⁻¹)

(11) rod

50
80%   30

-0.2   -0.1   0   0.1   0.2
(Å⁻¹)

Intensity (arb. units)

0    0.4    0.8    1.2    1.6
$q_z$ (Å⁻¹)
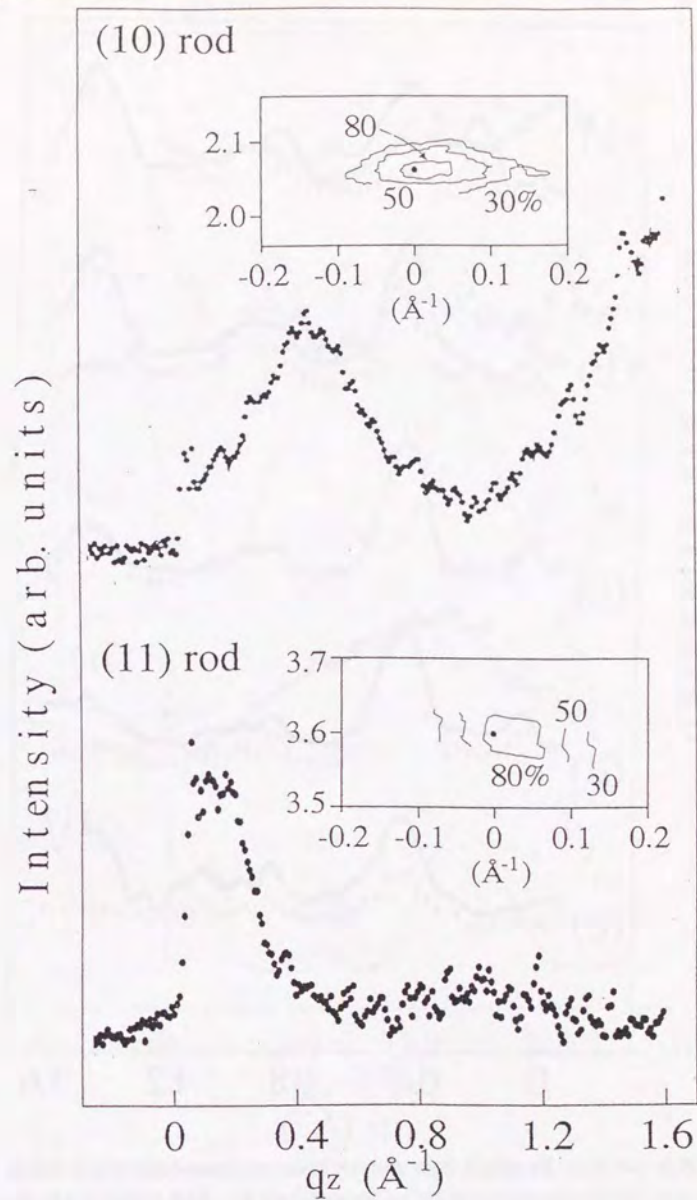
Fig. 5-4-7: Bragg rod profiles of (a) 10 rod and (b) 11 rod calculated from the scan shown in Fig. 5-4-5. Insets show the shapes of the Bragg rods by the contours at 100% (dots), 80%, 50%, and 30% of the maximum.
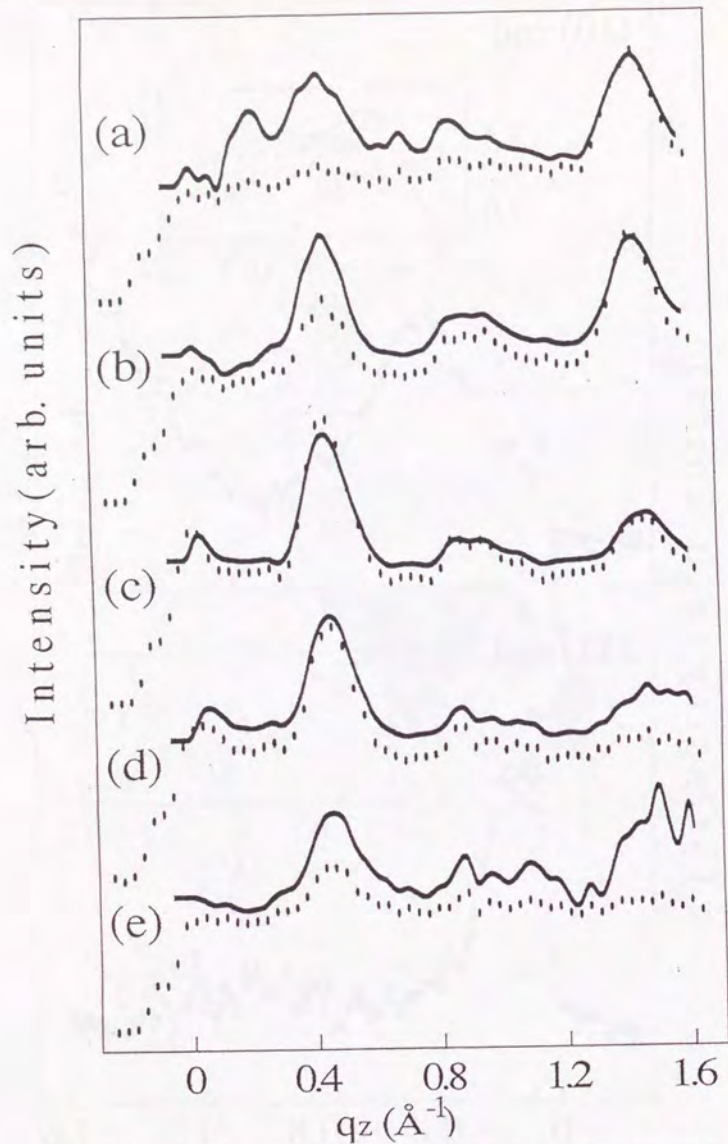
Fig. 5-4-8: Broken lines: raw diffraction intensities from $NbSe_2$ 7ML on HOPG detected by PSPC with different $\phi$. Solid lines: Modifications of the raw data for the derivation of BRP. (a) $\phi = 17.20°$, (b) $\phi = 17.28°$, (c) $\phi = 17.36°$, (d) $\phi = 17.44°$, (e) $\phi = 17.52°$. This procedure is necessary because HOPG substrate is made of rotated microcrystals. The determined Bragg rod profile is shown in Fig.5-4-11(a).
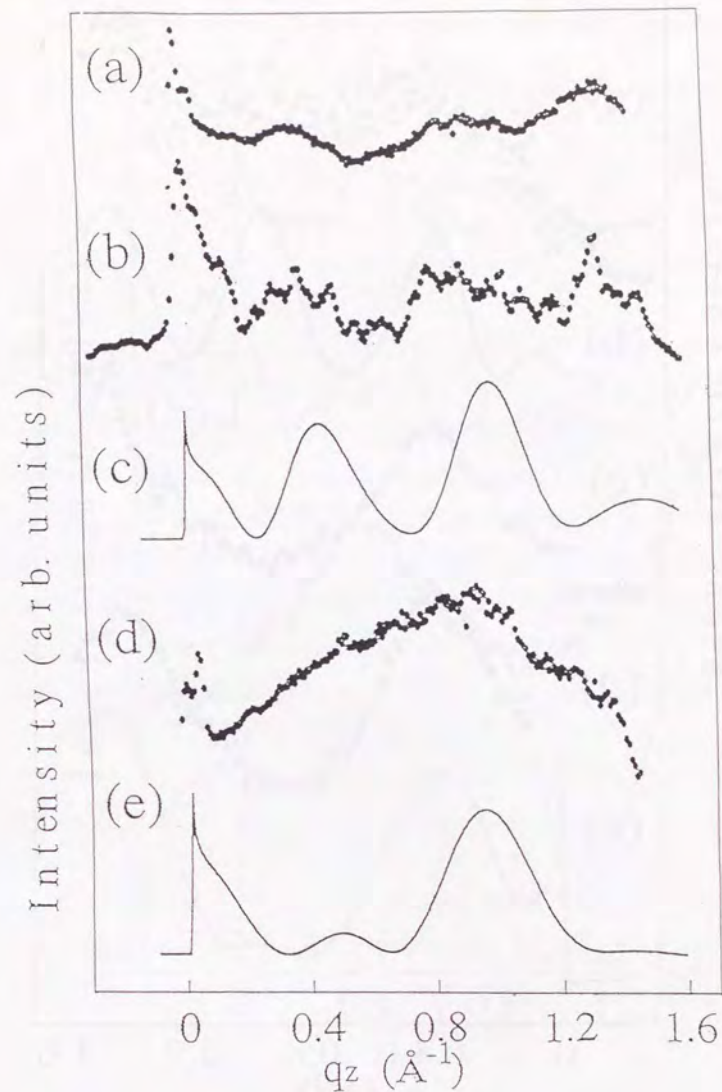


Fig 5-4-9: Growth temperature dependence of $TaSe_2$ films. Dotted curves: Bragg rod profile from $TaSe_2$ films on Se-GaAs. The substrate temperatures were: (a) 590°C, (b) 495°C, (d) 410°C. Solid lines: simulations by kinematical methods. The polytype, thickness and surface roughness are (c) 2Ha, 4ML, 0.8Å; (e) 1T, 3ML, 1.1Å, respectively.
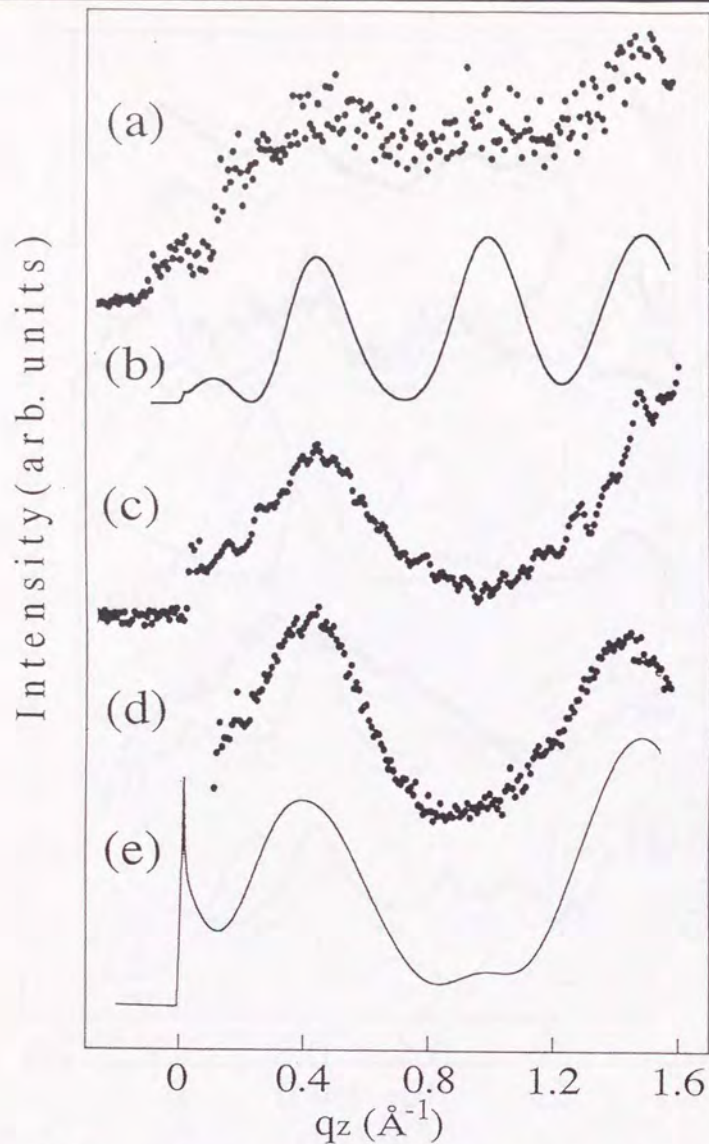
Fig. 5-4-10:  Growth temperature dependence of NbSe$_2$ films. Dotted curves: Bragg rod profile from NbSe$_2$ films on Se-GaAs. The growth temperature were: (a) 535°C, 11ML; (c) 500°C, 7ML; (d) 420°C, 7ML. Solid lines: simulations by kinematical methods. The polytype, thickness and roughness are (b) 2Ha, 4ML, 0Å; (e) 2Hb(50%)+3R(50%), 7ML, 0.61Å.  0.5% deviation of the layer spacing and ±1° corrugation of layers are assumed in (e).
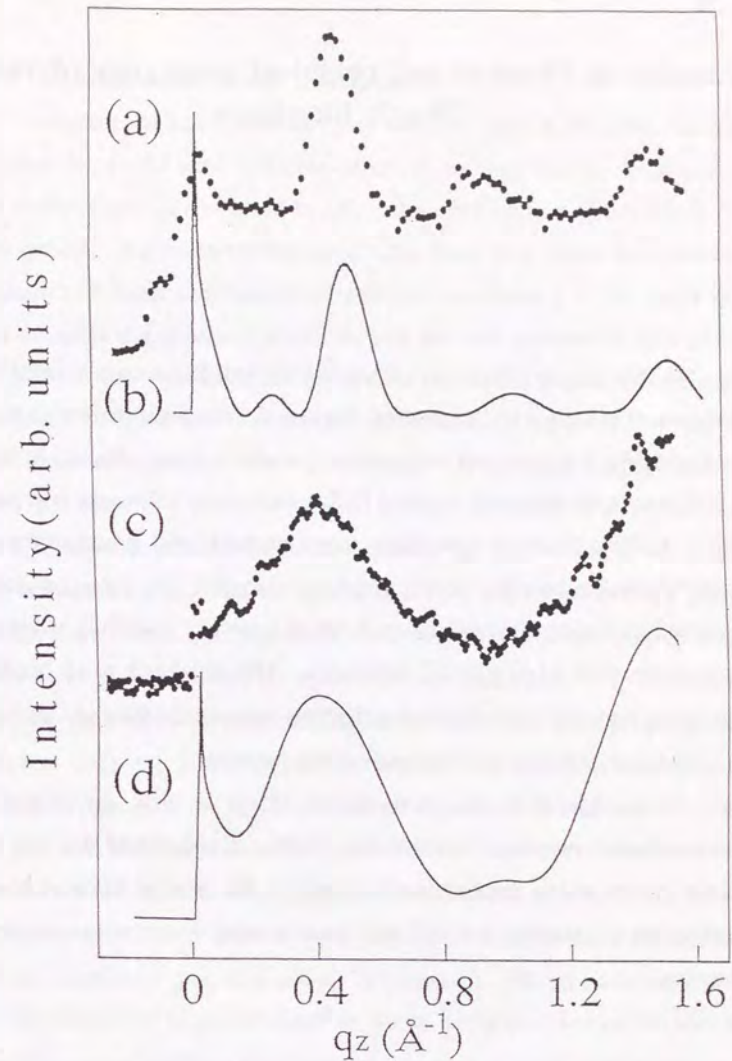


Fig. 5-4-11:  Substrate dependence of  10 Bragg rod profile from NbSe$_2$ films grown at 500°C with the thickness of 7ML. (a) a NbSe$_2$ film on HOPG (b) Simulation by a kinematical method. The polytype, thickness and roughness are 2Hb,  6ML,  and  0.85Å,  respectively.   (c) a film on Se-GaAs. (d) 2Hb(50%)+3R(50%), 7ML, 0.61Å.  0.5% deviation of the layer spacing and ±1° corrugation of layers are assumed in (d).